Transient, developmental exposure to patient-derived anti-NMDA receptor autoantibodies causes long-term axonal and behavioral defects

Jing Zhou[1,2,3], Ariele L. Greenfield[1,2*], Rita Loudermilk[1,2*], Christopher M. Bartley[2,3,4*], Baouyen T. Tran[1,2,3], Chao Zhao[5], Hong Wang[1,2], Michael R. Wilson[1,2,3], Samuel J. Pleasure[1,2,3,6]

*, equal contributions

1. Department of Neurology, University of California, San Francisco, San Francisco, CA 94143, USA.
2. Weill Institute for Neurosciences, University of California, San Francisco, San Francisco, CA 94143, USA.
3. Center for Encephalitis and Meningitis, University of California, San Francisco, San Francisco, CA 94143, USA.
4. Department of Psychiatry, University of California, San Francisco, San Francisco, CA 94143, USA.
5. Center for Data Driven Discovery in Biomedicine, Children's Hospital of Philadelphia, Philadelphia, Pennsylvania, PA 19146, USA.
6. Programs in Neuroscience and Developmental Stem Cell Biology, Eli and Edythe Broad Center of Regeneration Medicine and Stem Cell Research, Kavli Institute for Fundamental Neuroscience, San Francisco, CA 94143, USA.

Electronic address: samuel.pleasure@ucsf.edu

Abstract

NMDA receptor autoimmune encephalitis (NMDAR-AE) is characterized by cerebrospinal fluid (CSF)-resident anti-NMDA receptor autoantibodies that cause behavioral and neurologic deficits. Although many symptoms are responsive to immunotherapy, for many patients functionally impairing deficits persist. We used patient-derived GluN1 and GluN2A-specific monoclonal antibodies (mAbs) to interrogate the molecular and circuit basis for persistent sensory-motor deficits following NMDAR-AE. During postnatal development, intracortical injection of either mAb disrupted callosal circuit formation with excess callosal projections in primary somatosensory cortex (S1), although the anti-GluN1 antibody provoked the more severe phenotype. S1 circuit disruption during development results in permanent axon morphology alterations and sensory-motor deficits lasting to adulthood. The severity of sensory-motor deficits was correlated with the severity of axon morphology alterations, and these anatomic changes are associated with sensory-motor behavior deficits similar to those in children NMDAR-AE. Our studies provide a molecular, cellular, and circuit basis for persistent neuropsychiatric deficits in NMDAR-AE.

Introduction

Anti-NMDA receptor (anti-NMDAR) encephalitis is an increasingly recognized neuroinflammatory syndrome associated with antibodies against the extracellular domain of NMDAR, with a predilection for patients from childhood to young adulthood (1, 2). Patients typically present with psychosis followed by seizures, movement disorders, and impairment of short-term memory, which can lead to long-term morbidity or mortality. Continuous

ventricular infusion of patient cerebrospinal fluid (CSF) in adult mice recapitulates some aspects of the acute disease phenotype including memory and behavioral defects (3, 4). Other studies showed that anti-NMDAR antibodies lead to a selective and reversible decrease in NMDAR surface density and synaptic localization correlating with antibody titers (1, 5-7). However, it is hard to reconcile patients' slow recovery after effective treatment, if the only pathophysiologic change is a reversible loss in NMDAR surface density and synaptic localization. Lingering clinical deficits suggest that anti-NMDAR autoantibodies not only pharmacologically antagonize NMDAR-mediated neurotransmission but also impair circuit integrity (8). Most importantly, whether and how anti-NMDAR autoantibodies are sufficient to disrupt cellular morphology and cause persistent circuit and behavioral deficits is largely unknown.

Abnormal movements are seen in 90% of patients, especially children (9). Clinically, earlier age of exposure to the antibodies and longer delays (> 4 weeks) before treatment are associated with a more severe disease course, including a higher risk of persistent sensory-motor deficits (10). Sensory-motor coordination relies on somatosensory cortex communication through the corpus callosum (CC) (11). The CC is the largest interhemispheric commissural circuit in mammals, and CC connectivity is essential for bilateral coordination and higher cognitive processes (12). In humans, the general shape of the CC is present at birth, but the CC continues to develop throughout childhood and into adolescence (13-15). This prolonged period of CC development in humans (and rodents) suggests significant vulnerability of these forming circuits to environmental insults and make the CC an attractive structure to study in models of NMDAR-AE in development. To understand CC development and its key role in neurological diseases, we have advanced multi-site *in utero* electroporation to label callosal neurons with fluorophore in any given cortical regions and developed quantitative imaging methods for tracing single callosal axon projections over long distances in mouse models (16).

We demonstrated previously that genetic disruption of NMDAR and commercial antibody-mediated loss of function lead to defects of callosal projections in primary somatosensory cortex (S1) in mice, and that NMDAR-dependent EPHRIN-B/EPHB signaling likely mediate this phenotype (8). However, whether patient-derived, pathogenic anti-NMDAR autoantibodies cause these defects and are associated with irreversible sensory-motor circuit disruption with attendant behavioral deficits are unknown. If so, developmental exposure to anti-NMDAR antibodies in patients has important implications for the course and long-term morbidity of children with anti-NMDAR encephalitis, even after successful treatment of the acute illness.

Here, we generated anti-GluN1 and anti-GluN2A human monoclonal antibodies (mAbs) from CSF B-cells isolated from a patient with recurrent anti-NMDAR encephalitis. We used these patient-derived mAbs to study the long-term consequences of transient developmental NMDAR disruption on axonal morphology, callosal circuity, and behavior.

Results

Generation and validation of patient-derived monoclonal anti-NMDAR antibodies

We isolated single, antigen-experienced B-cells from the CSF of a patient experiencing recurrent anti-NMDAR encephalitis using a piezoacoustic liquid handling device (Cellenion, Lyon, France and SCIENION, Berlin, Germany) adapted for highly efficient single cell isolation. After RNA extraction and RT-PCR of the heavy and light chains of the immunoglobulin gene, we Sanger sequenced the amplicons and produced four distinct patient-derived human IgG1 mAbs using published approaches (17, 18) (**Figure 1A**).

Immunoprecipitation (IP) with adult mouse brain lysate showed that patient CSF IgG and two of these mAbs (mAb1 and mAb3) bound NMDAR complexes (**Figure 1B**). Comparing with the negative control (**Figure 1C**), immunostaining of mouse brain tissue with patient CSF IgG, mAb1, and mAb3 produced characteristic intense neuropil staining in the hippocampus (**Figures 1D-1F**) (2, 5, 19). Immunostaining live murine hippocampal neurons with mAb1 and mAb3 from *Emx1*$^{cre/+}$; *Grin1*$^{wt/wt}$; *Rosa26*$^{fs\text{-}tdTomato}$ mice, produced punctate cell-surface staining, where red fluorescence marks Cre-mediated recombination without deletion of NMDAR (**Figures 1G**, **1H**). The punctate cell-surface staining was lost in red cells of *Emx1*$^{cre/+}$; *Grin1*$^{fl/fl}$; *Rosa26*$^{fs\text{-}tdTomato}$ cultures (**Figure 1I**), which mark the individual NMDAR knock-out (KO) neurons with red fluorescent protein tdTomato, suggesting that mAb1 and mAb3 directly bind NMDAR and recognized extracellular epitopes of NMDAR.

Interestingly, unlike the uniform staining pattern of mAb3 (**Figure 1F**), the staining of mAb1 was more prominent in olfactory bulb, cortex, and hippocampus (**Figures 1E**). Even though both mAbs showed punctate neuropil staining in dissociated cells, mAb3 staining was more dispersed and it was also seen prominently in neuronal cell bodies and processes (**Figure 1J**). In addition, strong staining for mAb3 was seen in postnatal day (P) 8 mouse brain, while faint and weak staining for mAb1 was present in P8 mouse brain (**Figure S1**). These different spatial and temporal patterns along with the fact that both mAbs immunoprecipitated NMDAR and associated proteins suggested they may recognize different subunits of NMDAR.

mAb3 binds the GluN1 subunit, while mAb1 binds the GluN2A subunit

NMDARs are heteromeric receptor Ca^{++} channel complexes with various subunit compositions. To date, seven different subunits have been identified: the GluN1 subunit, four distinct GluN2 subunits (A-D), and two GluN3 subunits. The GluN1 subunit is required for all functional NMDARs (20, 21). In the forebrain, GluN1 primarily assembles with GluN2A and GluN2B to form functional NMDARs. GluN2A- and GluN2B-containing NMDARs follow different developmental expression trajectories with GluN2B as the major NR2 subunit during the first postnatal week and GluN2A expression present but increasing thereafter (22-25). According to the uniform staining pattern of mAb3 during development and in adulthood (**Figures 1F and S1**), we hypothesized that mAb3 may recognize the GluN1 subunit. The weak staining of mAb1 during development (**Figure S1**) with strong

staining in adulthood (**Figure 1E**), as well as its distinct staining pattern in forebrain (**Figure 1E**), suggested that mAb1 may recognize the GluN2A subunit.

To determine the subunit specificity of mAb1 and mAb3, we evaluated staining patterns in GluN1 KO, GluN2A KO, and GluN2B KO mice. In *Emx1*$^{cre/+}$; *Grin1*$^{fl/fl}$; *Rosa26*$^{fs\text{-}tdTomato}$ mice, the GluN1 subunit was knocked out and all NMDARs failed to assemble in red cells. Consistent with our results shown in **Figure 1**, in brain sections from control *Emx1*$^{cre/+}$; *Grin1*$^{wt/wt}$; *Rosa26*$^{fs\text{-}tdTomato}$ mice, mAb1 staining was mostly present in neuropil but less on cell bodies; while mAb3 staining was both detected in neuropil and on cell bodies (**Figure 2Bi**). However, the punctate staining of mAb1 was dramatically decreased in brain sections of *Emx1*$^{cre/+}$; *Grin1*$^{fl/fl}$; *Rosa26*$^{fs\text{-}tdTomato}$ mice (**Figures 2Bii, 2C and 2D**) and somatic staining of mAb3 was completely lost in red (recombined) cells of *Emx1*$^{cre/+}$; *Grin1*$^{fl/fl}$; *Rosa26*$^{fs\text{-}tdTomato}$ brain sections (**Figures 2Bii and 2E**), further confirming our impression that the two mAbs directly bind NMDAR. Next, we examined their staining pattern in *Emx1*$^{cre/+}$; *Grin2A*$^{fl/fl}$ mice, lacking GluN2A-containing NMDARs in excitatory cortical neurons. Compared with brain sections of control *Grin2a*$^{fl/fl}$ mice, the punctate fiber staining of mAb1 in *Emx1*$^{cre/+}$; *Grin2a*$^{fl/fl}$ mice was significantly decreased (**Figures 2Fi, 2Fii and 2G**, $P<0.0001$). However, there was no difference between mAb3 staining in these mice (**Figures 2Fi, 2Fii and 2H**). These results suggested that mAb1, but not mAb3, directly binds to the GluN2A subunit of NMDAR. Then, we examined their staining pattern in *Emx1*$^{cre/+}$; *Grin2b*$^{fl/fl}$; *Rosa26*$^{fs\text{-}tdTomato}$ mice, in which GluN2B-containing NMDARs were deleted in red cells. There was no difference in the staining for either mAb1 or mAb3 in brain sections of *Emx1*$^{cre/+}$; *Grin2b*$^{fl/fl}$; *Rosa26*$^{fs\text{-}tdTomato}$ and control *Emx1*$^{cre/+}$; *Grin1*$^{wt/wt}$; *Rosa26*$^{fs\text{-}tdTomato}$ mice (**Figures 2I-2K**). This suggests that neither of the two mAbs bind to the GluN2B subunit of NMDAR. Since mAb3 did not directly bind to either GluN2A or GluN2B subunits, but bound to NMDAR, mAb3 must bind directly to the GluN1 subunit of NMDAR. Taken together, these results suggested that mAb3 binds the GluN1 subunit, while mAb1 binds the GluN2A subunit.

mAb1$^{[GluN2A]}$ and mAb3$^{[GluN1]}$ injection disrupt callosal innervation in primary somatosensory cortex

The callosal innervation pattern of primary somatosensory cortex (S1) in mice reveals initial diffuse projection to S1 at P8, with refinement of the innervation at the primary somatosensory cortex/secondary somatosensory cortex (S1/S2) border at P14. We previously demonstrated that NMDAR in the target S1 controls the pattern and terminal density of afferent callosal axonal projections (8)[i] by showing that genetic and commercial antibody-mediated loss of function of NMDAR in contralateral target S1 but not in ipsilateral projecting S1 causes diffuse and more overall callosal axons innervating S1 at P14. This phenotype is not mediated by the ion channel function of NMDAR but instead mostly depends on the interactions between NMDAR and the axon guidance signaling pathway EPHRIN-B/EPHB.

To test whether exposure to human pathogenic anti-NMDAR autoantibodies disrupts commissural S1 circuit formation, we separately injected the two patient-derived mAbs into mice during callosal development. We first

labelled layer II/III callosal neurons by *in utero* electroporation of progenitor cells with enhanced green fluorescent protein (EGFP) at embryonic day (E) 15.5 (**Figure 3A**). Then we injected the mAbs in the contralateral target S1, twice-daily from P3 to P12, and examined the callosal innervation pattern at P14 (**Figures 3B-3D**). The feasibility and efficiency of this cortical antibody injection has been demonstrated in our previous study (8). Injection of mAb3$^{[GluN1]}$ led to a diffuse termination pattern and significant increase in the callosal innervation in contralateral S1 at P14 relative to control human IgG (**Figure 3D and 3E**, P = 0.01). Injection of mAb1$^{[GluN2A]}$ also slightly increased callosal innervation in contralateral S1 at P14 (**Figures 3C and 3E**), results consistent with our genetic data showing that the effects of *Grin2A* loss-of-function were milder than *Grin1* loss-of-function (8). Importantly though, our results also support potential pathologic effects of GluN2A autoantibodies during development, which hasn't been demonstrated previously.

We next used quantitative immunofluorescence to determine whether, like genetic NMDAR disruption, patient-derived mAbs alter the EPHRIN/EPH pathway. We found that the expression of EPHB2 was dramatically reduced in mAb3$^{[GluN1]}$-treated S1, but not in mAb1$^{[GluN2A]}$-treated S1 (**Figures 3F-3H**). This is consistent with our own genetic data (8), but also with previous data that indicate that EPHB2 interacts with NMDAR via GluN1 and not GluN2A (26, 27) .

Permanent alterations of S1 callosal axons in mice exposed transiently to mAbs during development

To determine if the early, transient exposure to antibodies resulting in callosal circuit disruption last to adulthood, we anatomically examined the S1 callosal circuit at P120. Interestingly, by P120, the excess S1 callosal innervation seen in mice treated with mAbs during development had resolved (**Figures 4A and 4B**), but we also assessed cell morphology at the single-cell level by tracing individual callosal axon terminals in S1 (**Figures 4C, S2**, **Materials and methods**) and assessing morphometric features, including terminal field areas, numbers of branch points and terminal points, total branch length, branch diameter, branch resistance, branch levels, branch angles, and branch orientations.

Unexpectedly, axon terminal morphology in S1 remained altered in mAb-treated mice in a sex-specific manner months after the transient exposure to antibody (**Table 1**). mAb1$^{[GluN2A]}$-treated females and mAb1$^{[GluN2A]}$- and mAb3$^{[GluN1]}$-treated males displayed significantly higher numbers of axon branch crossings using Sholl analysis (**Figures 4D and 4J**), suggesting increased branch complexity and larger terminal field areas (28). mAb3$^{[GluN1]}$-treated female and male mice displayed significantly increased axon branch points, terminal points, and total branch length (**Figures 4E-4G and 4K-4M**), consistent with higher branch complexity. Importantly, mAb1$^{[GluN2A]}$- and mAb3$^{[GluN1]}$-treated male mice also displayed significantly reduced branch diameter (**Figure 4N**), but increased axon resistance (**Figure 4O**), suggesting lower conduction velocity in signal propagation. In addition, mAb3$^{[GluN1]}$ male mice displayed significantly increased axon branch levels (**Figure 5D**), branch angles (**Figure S3**), and altered branch orientation angles (**Figures 5E and 5F**). As shown in **Figure 4C**, most axon

branches should be directed toward the pia at the cortical surface. However, many axon branches in mAb3$^{[GluN1]}$ male mice branch away from the cortical surface, leading to reduced branch orientation angle (**Figures 5E and 5F**). This altered axonal geometry suggests slowed signal conduction and increased possibility of signal propagation failures along axon branches (29).

Persistent sensory-motor deficits in mice treated with patient-derived mAbs during development

Callosal projection in S1 is essential for bilateral sensory-motor integration (**Figure S4A**). The callosal axon terminals in S1 are the key structures to propagate and coordinate bilateral sensory signal conduction. These morphological alterations of reduced axon diameter, increased branch complexity, or altered geometry in axon terminals (**Table 1**), all could slow down the sensory signal conduction, cause delayed sensory processing and poor sensory-motor integration (**Figure S4B**). Thus, we wondered whether these persistent morphological alterations could cause lasting sensory-motor deficits.

Thus, we performed a battery of behavioral tests in mice from 1- to 4-months-old. To assess overall motor activity levels, we measured baseline anxiety using an elevated plus maze (EPM), and baseline locomotor activity with the repeated open field test (OFT). Time spent in the open arms of EPM (**Figure S5**), which measures anxiety-like behavior, along with distance traveled in the EPM (**Figure S5**), were similar among the groups. Total movements in the OFT (**Figures 6A and 6B**), which measures locomotor activity, were also similar among groups. These indicated that mAb treated animals and controls had similar levels of anxiety and overall locomotor activity.

Next, we performed a battery of more specific sensory-motor tasks. In measures of coarse movement function - burrowing test (**Figures 6C and 6D**) (measuring digging and kicking activity) and rotarod (**Figures 6E and 6F**) (measuring sensory-motor coordination), mice showed comparable performance among the groups. In contrast, mAb treated mice showed impairments in fine motor tasks, including nest building (30), balance beam and the facing upward pole test (**Figures 7, Video S1-S12**). Generally, in these tasks of more fine motor-sensory integration, mAb3$^{[GluN1]}$-treated mice were more severely affected than mAb1$^{[GluN2A]}$-treated mice. Surprisingly, we also observed sex-differences in these fine motor impairments (**Table 2**).

Specifically, mAb3$^{[GluN1]}$-treated male mice showed significantly impaired nest building (**Figures 7B**); mAb3$^{[GluN1]}$-treated female (**Figures 7D, Video S3**) and mAb1$^{[GluN2A]}$-treated male mice (**Figures 7F, Video S5**) showed significantly increased balance check; mAb3$^{[GluN1]}$-treated female (**Figures 7L, Video S9**), mAb1$^{[GluN2A]}$- and mAb3$^{[GluN1]}$-treated male mice (**Figures 7M, Videos S11 and S12**) showed significantly extended descending time in the facing upward pole test. There was no correlation between motor performance and body weight, muscular strength, or coordination (**Figure S6-S9**). These results demonstrate that developmental exposure to pathogenic anti-NMDAR autoantibodies result in persistent fine sensory-motor deficits in mice. Most interestingly, the morphological alterations of S1 callosal axons were highly and positively correlated with the behavioral

deficits in sensory-motor coordination. mAb3$^{[GluN1]}$-treated male mice with most altered morphology in S1 axon terminals displayed the worst behavioral performance in sensory-motor coordination (**Tables 1 and 2**).

Discussion

Important advances have been made in understanding the pathophysiology of anti-NMDAR encephalitis during the acute phase (31). However, despite initial responsiveness to immunotherapy, these patients are often left with residual cognitive deficits and behavioral abnormalities that can last for months or years (32, 33), the basis of which is not well-understood. Here, using the somatosensory callosal circuit as a model, we show that transient, developmental exposure to patient-derived anti-NMDAR autoantibodies results in long-lasting morphometric and physiologic axonal defects. These cellular and physiologic perturbations are read out as persistent functional deficits in fine sensory-motor tasks. This is relevant to the effects of this syndrome in pediatric and newborn patients and suggests a basis for the protracted neurocognitive deficits observed in anti-NMDAR encephalitis patients even after resolution of the acute phase of the illness when titers of the autoantibodies have decreased (34).

Clinical observations support our experimental conclusions that developmental exposure to anti-NMDAR antibodies can cause persistent circuit deficits even long after definitive treatment leading to diminished autoantibody levels. Functional magnetic resonance imaging (fMRI) studies revealed altered functional connectivity, including significant reductions in sensory-motor connectivity, in a cohort of anti-NMDAR encephalitis patients after the acute stage of the disease (35, 36). A structural brain MRI study in a cohort of pediatric anti-NMDAR encephalitis patients found significant brain volume loss and failure of age-expected brain growth. In this cohort, the abnormal MRI findings, a clinical presentation with sensory-motor deficits, and a treatment delay > 4 weeks were associated with a worse clinical outcome (10). Moreover, a 10-year follow-up of an anti-NMDAR encephalitis patient who presented with a dysexecutive syndrome showed persistent electroencephalographic abnormalities in the brain (37).

Autoantibodies against different NMDA receptor subunits have been identified (38-40). Specifically, autoantibodies against the GluN1 subunit of NMDAR are thought to be the primary pathogenetic autoantibodies in anti-NMDAR encephalitis (41). Consistent with this, we found that injection of a patient-derived anti-GluN1 mAb into the cortex during a critical developmental period significantly decreased the expression of EPHB2 in *vivo* (**Figures 3F-3H**), disrupted individual neuron morphologies (**Figures 4, 5 and S3**), altered cortical circuits (**Figures 3**), and impaired behavior performance (**Figures 7**).

In contrast, anti-GluN2 autoantibodies have been reported in patients with diseases ranging from stroke to neuropsychiatric lupus and autism spectrum disorders, but it is less clear whether they play a pathogenic role (42-45). We also cloned an autoantibody against GluN2A subunit of NMDAR from the anti-NMDAR encephalitis

patient and found that injection of this anti-GluN2 mAb into the cortex led to a clear phenotype during the same critical developmental period. While similar in some respects, the anti-GluN2A mAb caused less severe alterations in individual neuron morphologies, cortical circuits, and behavioral changes (**Figures 3-7, S3**) than the anti-GluN1 mAb. In summary, this is the first unequivocal demonstration of the pathologic effects of pathogenic anti-GluN2A autoantibodies in anti-NMDAR encephalitis patients and suggests that further study of antibody specificity and function in the other conditions associated with anti-GluN2A autoantibodies is necessary.

Coordination of the hands and fingers relies on communication through the CC in somatosensory cortex (11, 46). Each subcortical somatosensory neuron responds to specific stimuli applied to a specific region of the body. The stimulated body area capable of evoking a response of a given somatosensory neuron is called the neuron's receptive field (RF). As proven in our mouse models, it is possible that in young children or during fetal development, anti-NMDAR autoantibodies may cause irreversible morphological alterations with higher branch complexity, increased axon resistance and altered branch orientation angles of callosal axon terminals in somatosensory cortex (**Figures 4, 5 and S3**), which could slow signal propagation, disrupt sensory-motor integration, and lead to persistent sensory-motor deficits in children. In addition, the higher branch complexity and larger terminal field of S1 callosal neurons may give rise to larger and diffuse receptive fields in S1, less precise perception but sensory overload of afferent somatosensory inputs. Psychiatric deficits (e.g., anxiety and aggression) are very common in patients with anti-NMDAR encephalitis (1). In patients, the feeling of anxiety may arise from sensory overload (47). In the future, it would be interesting to investigate how the neuronal morphology and circuit changes induced by anti-GluN1 and GluN2A autoantibodies contribute to the neuropsychiatric disorders in these patients.

In the developing nervous system, neurons produce exuberant processes. During the early postnatal period, these excessive connections are removed through synapse elimination by glial cells (48, 49). Studies indicate that glial cells may play a major role in the generation of sex-differences in the deficits in brain function caused by pathology (50). Sex-differences of individual callosal neuron morphology and behavior deficits were observed in our mouse models (**Tables 1 and 2**). mAb3$^{[GluN1]}$-treated male mice with most altered morphology in S1 axon terminals displayed the worst behavioral performance in sensory-motor coordination. It is possible that endogenous differences in the protective and reparative actions of female and male glial cells contribute to the generation of sex-differences in our mouse models. What causes the sex-differences, and whether and how glial cells are involved in these processes, need to be further investigated.

In this study, we generated and characterized monoclonal anti-GluN1 and anti-GluN2A autoantibodies from a patient with anti-NMDAR encephalitis and assessed their ability to disrupt sensory-motor circuits in a well characterized mouse model of callosal circuit formation. We found a central role of anti-GluN1 and anti-GluN2A autoantibodies in the pathogenesis of anti-NMDA receptor encephalitis; uncovered the different effects of these autoantibodies on callosal circuit formation, individual callosal axon morphologies and behavioral measures; and

revealed the potential mechanisms of circuit disruptions underlying the persistent behavior deficits in anti-NMDAR encephalitis.

Acknowledgements

We thank Jeffrey Simms in Gladstone Behavior Core for helping with experimental design and data analysis on behavior tests. We thank Dan Wang in Dr. Dena Dubal's lab at UCSF for helping with behavior tests and data analysis. We thank Wenjie Mao in Dr. Lennart Mucke's lab at Gladstone Institute for discussing on behavior tests. We thank Blaise Ndjamen in Gladstone Histology and Light Microscopy Core for helping with confocal imaging and Imaris data analysis. The work has also been supported by R56 MH119435 (SJP), NIH/NIMH R01MH122471 (SJP, MRW), UCSF Weill Institute for Neurosciences Innovation Award (SJP, MRW), Marcus Program in Precision Medicine Innovation Transformative Integrated Research Initiative (SJP, MRW), and the Program for Breakthrough Biomedical Research New Frontiers Research Award (SJP, MRW) which is partially funded by the Sandler Foundation. C.M.B is supported by the Hanna H. Gray Fellowship, HHMI and University of California President's Postdoctoral Fellowship Program. A.L.G. was supported by the NMSS Clinician-Scientist Development Award, Kathleen C. Moore Postdoctoral Fellowship. We thank the patient for his participation in research.

Author contributions

J.Z. and S.J.P designed the experiments. J.Z., C.M.B., and B.T. performed experiments. A.L.G., R.L. and M.R.W. developed the efficient single cell isolation protocol, isolated the patient's CSF B-cells and made the patient-derived monoclonal anti-NMDAR antibodies. C.M.B., R.L. B.T. and J.Z. verified these antibodies. J.Z. performed all mouse surgeries, behavior tests, anatomy and single neuronal, morphology analysis. J.Z., C. Z., H. W. analyzed the data. J.Z., C.M.B., M.R.W and S.J.P wrote the manuscript.

Declaration of interests

Christopher Bartley has received an honorarium for speaking to the Commonwealth Club and hold shares in NowRx Inc.

Figures and Figure legends

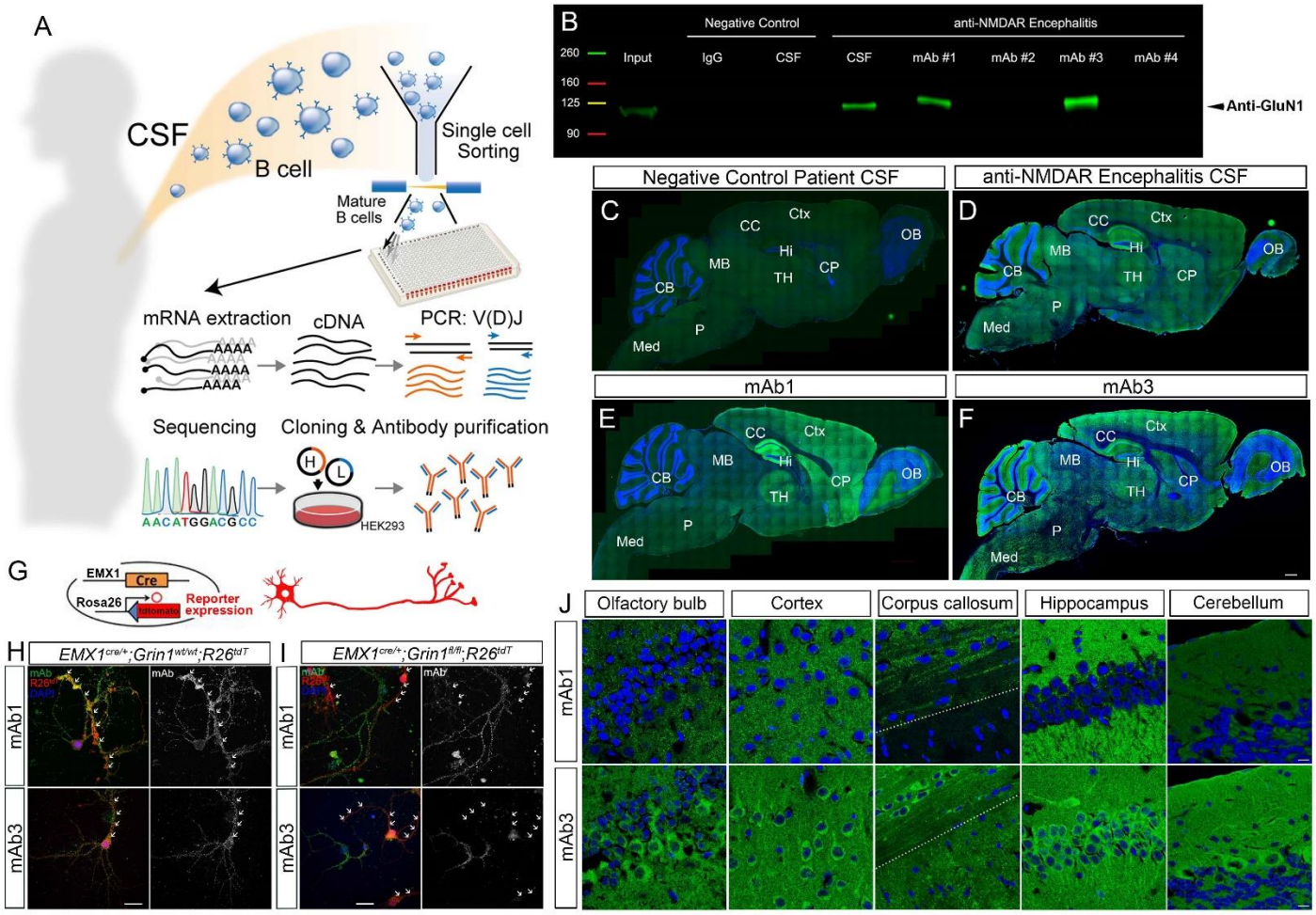

Figure 1: **Generation of patient-derived monoclonal anti-NMDAR antibodies.** (A) Diagram of generation of patient-derived monoclonal anti-NMDAR antibodies. (B) Immunoprecipitation of GluN1 from postnatal day 40 (P40) mouse brain homogenates by using anti-NMDAR encephalitis patient's CSF, mAb1, mAb2, mAb3 and mAb4. Immunoprecipitation with human IgG, nonanti-NMDAR encephalitis patient's CSF served as negative controls. (C-F) Immunostaining with CSF of negative control patient (C), CSF of anti-NMDAR encephalitis patient (D), mAb1 (E) and mAb3 (F) on sagittal sections of P40 mouse brains. The staining of control patient CSF served as negative control. (G-I) mAb1 and mAb3 recognized extracellular epitopes of NMDAR. (G) We crossed *Emx1*$^{cre/+}$; *Grin1*$^{fl/fl}$ mice with Cre-reporter *Rosa26*$^{fs\text{-}tdTomato}$ mice to produce GluN1 knockout cells labled with red fluorescence. Hippocampal neurons were cultured from *Emx1*$^{cre/+}$; *Grin1*$^{fl/fl}$; *Rosa26*$^{fs\text{-}tdTomato}$ mice. Hippocampal cultures of *Emx1*$^{cre/+}$; *Grin1*$^{wt/wt}$; *Rosa26*$^{fs\text{-}tdTomato}$ mice served as controls. (H, I) mAb1 and mAb3 showed punctate membrane staining in live staining of cultured hippocampal neuron. The staining was gone in red cells of *Emx1*$^{cre/+}$; *Grin1*$^{fl/fl}$; *Rosa26*$^{fs\text{-}tdTomato}$ cultures (I) but not red cells of *Emx1*$^{cre/+}$; *Grin1*$^{wt/wt}$; *Rosa26*$^{fs\text{-}tdTomato}$ cultures (H). (J) Immunostaining pattern of mAb1 and mAb3 in different brain regions. Dash line is the border line between cortex

and corpus callosum. Scale bar: 50μm for images in D and E; 500μm for images F, G and H; 10μm for images in I. *R26*^{tdT}: *Rosa26*$^{fs\text{-}tdTomato}$. OB: olfactory bulb. Ctx: cortex. Hi: hippocampus. CP: Caudoputamen. TH: thalamus. MB: midbrain. CB: cerebellum. P: pons. Med: medulla.

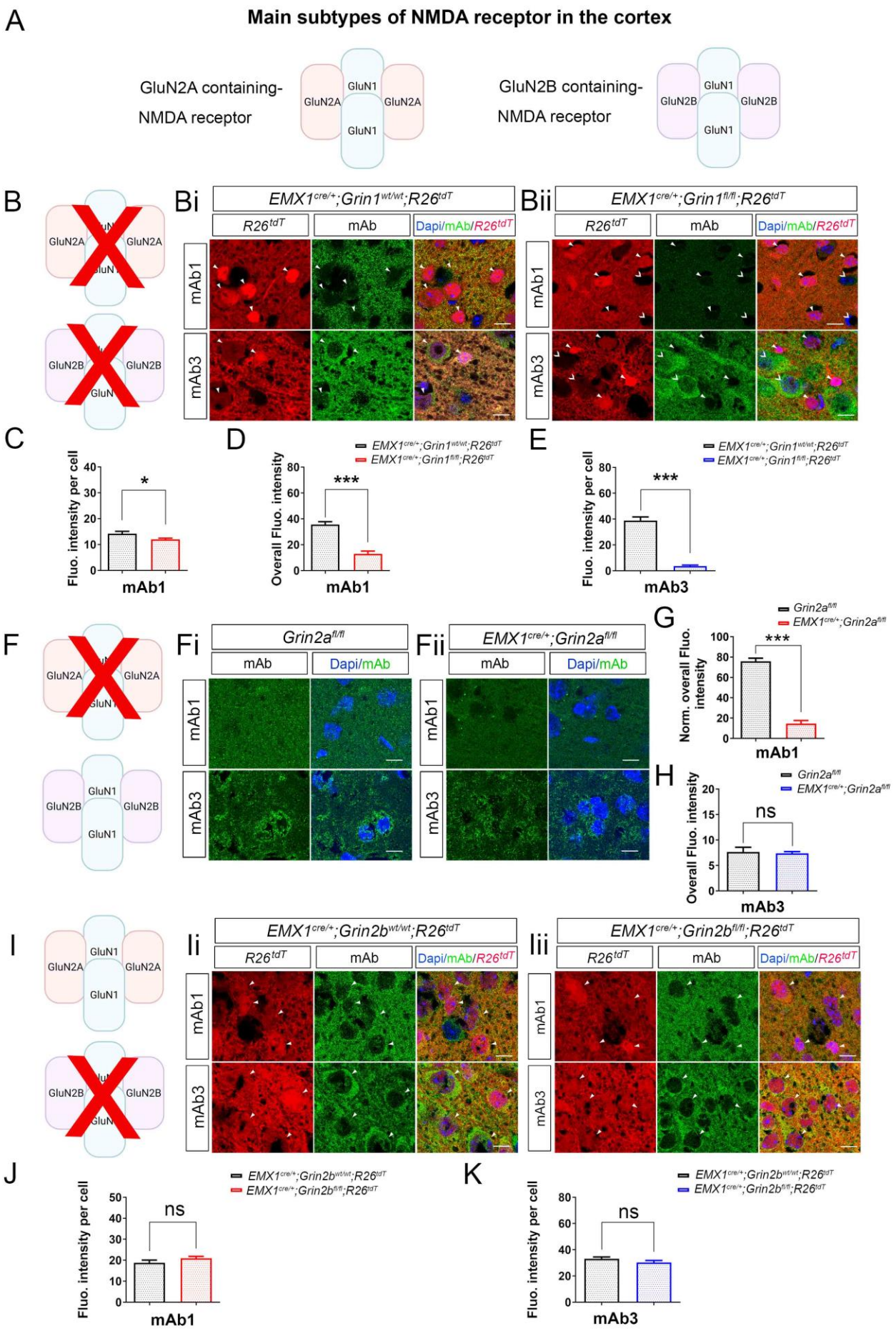
A
Main subtypes of NMDA receptor in the cortex
GluN2A containing-
NMDA receptor
GluN2B containing-
NMDA receptor
GluN1
GluN2A
GluN2B
B
Bi
Bii
EMX1cre/+;Grin1wt/wt;R26tdT
EMX1cre/+;Grin1fl/fl;R26tdT
R26tdT
mAb
Dapi/mAb/R26tdT
mAb1
mAb3
C
D
E
Fluo. intensity per cell
Overall Fluo. intensity
EMX1cre/+;Grin1wt/wt;R26tdT
EMX1cre/+;Grin1fl/fl;R26tdT
mAb1
mAb3
F
Fi
Fii
Grin2afl/fl
EMX1cre/+;Grin2afl/fl
Dapi/mAb
G
H
Norm. overall Fluo. intensity
ns
I
Ii
Iii
EMX1cre/+;Grin2bwt/wt;R26tdT
EMX1cre/+;Grin2bfl/fl;R26tdT
J
K
EMX1cre/+;Grin2bwt/wt;R26tdT
EMX1cre/+;Grin2bfl/fl;R26tdT

Figure 2: **mAb3 is against GluN1 subunit, while mAb1 is against GluN2A subunit**. (A) Diagram of GluN2A-containing NMDAR and GluN2B-containing NMDAR. (B-E) We generated *Emx1*$^{cre/+}$; *Grin1*$^{fl/fl}$; *Rosa26*$^{fs\text{-}tdTomato}$ mice to produce NMDAR knockout cells labled with red fluorescence. *Emx1*$^{cre/+}$; *Grin1*$^{wt/wt}$; *Rosa26*$^{fs\text{-}tdTomato}$ mice of the same litter served as control. Immunostaining of mAb1 and mAb3 were done in these brain sections (Bi, Bii). Triangle arrowheads pointed cells with Cre recombination. V shaped arrowheads pointed cells without Cre recombination. The punctate cell membrane and fiber staining of mAb1 were seen in *Emx1*$^{cre/+}$; *Grin1*$^{wt/wt}$; *Rosa26*$^{fs\text{-}tdTomato}$ mice (Bi), but dramatically reduced in *Emx1*$^{cre/+}$; *Grin1*$^{fl/fl}$; *Rosa26*$^{fs\text{-}tdTomato}$ mice (Bii). mAb3 signals were only detected on non-Cre recombination cells but absent on Cre recombination cells with deletion of NMDAR (Bii). (C, D) Quantification of fluorescence intensity of mAb1 immunostaining in single cells (C, P=0.03, n = 20 to 22 per group) and overall image (D, P<0.0001, n = 6 to 7 per group). (E) Quantification of fluorescence intensity of mAb3 immunostaining in single cells (P<0.0001, n = 20 to 21 per group). (F-H) We generated *Emx1*$^{cre/+}$; *Grin2a*$^{fl/fl}$ mice to conditional knock out GluN2A-containing NMDAR in excitatory neurons in cortex. The same littermates *Grin2a*$^{fl/fl}$ mice served as controls. The punctate staining of mAb1 seen in *Grin2A*$^{fl/fl}$ mice were dramatically reduced in *Emx1*$^{cre/+}$; *Grin2a*$^{fl/fl}$ mice (Fii, G (P<0.0001, n = 11 to 12 per group)). However, there were no difference between the signals of mAb3 in *Grin2a*$^{fl/fl}$ mice (F) and *Emx1*$^{cre/+}$; *Grin2a*$^{fl/fl}$ mice (Fii, H (P=0.79, n = 9 to 10 per group)). (I-K) We generated *Emx1*$^{cre/+}$; *Grin2b*$^{fl/fl}$; *Rosa26*$^{fs\text{-}tdTomato}$ mice to produce GluN2B-containing NMDARs knockout cells labled with red fluorescence. The littermates *Emx1*$^{cre/+}$; *Grin2b*$^{wt/wt}$; *Rosa26*$^{fs\text{-}tdTomato}$ mice served as controls. There were no difference between the singals of mAb1 (J, P=0.18, n = 25 to 26 per group) and mAb3 (K, P=0.16, n = 22 to 24 per group) in *Emx1*$^{cre/+}$; *Grin2b*$^{wt/wt}$; *Rosa26*$^{fs\text{-}tdTomato}$ mice (Ii) and *Emx1*$^{cre/+}$; *Grin2b*$^{fl/fl}$; *Rosa26*$^{fs\text{-}tdTomato}$ mice (Iii). Scale bar: 10μm for all images.

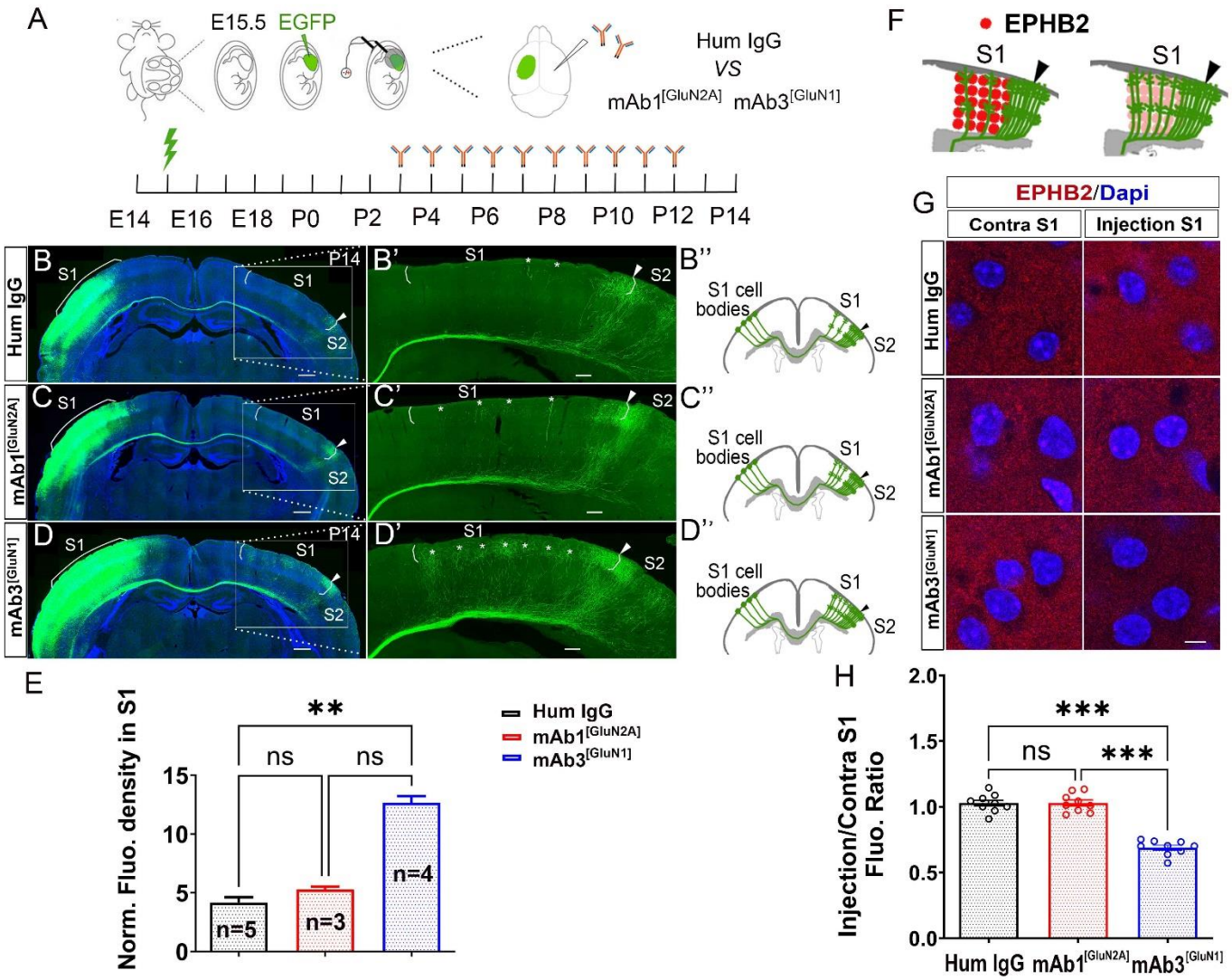

Figure 3: **Disrupted callosal innervation in primary somatosensory cortex (S1) after intraventricular injection of mAb1[GluN2A] and mAb3[GluN1] from P3 to P12.** (A) Diagram of experimental procedure. EGFP plasmid injected into lateral ventricle of embryo at embryonic day15.5 (E15.5) and electrical pulse given to enable the plasmid to enter cortical progenitor cells of layer II/III in the ventricular zone. mAb1[GluN2A] and mAb3[GluN1] were injected into the lateral ventricle from P3 to P12 in contralateral cortex. Human IgG served as control. Compared with control (B), mAb1[GluN2A] injection in mice showed slightly increased callosal innervation (C), but mAb3[GluN1] injection mice showed dramatically increased callosal innervation (D) in S1 at P14. "*" pointed the callosal axons in S1. (E) Quantification of fluorescence density. Human IgG *VS* mAb1[GluN2A]: P = 0.80. Human IgG *VS* mAb3[GluN1]: P = 0.01. mAb1[GluN2A] *VS* mAb3[GluN1]: P = 0.39. n = 3 to 5 per group. (F) Diagram of EPHB2 expression in S1. (G) Expression of EPHB2 in S1 of injecting side and contralateral noninjecting side for the three different treatments. (H) Quantification of fluorescence intensity ratio of injecting side to contralateral

noninjecting side. Human IgG *VS* mAb1[GluN2A]: P >0.999. Human IgG *VS* mAb3[GluN1]: P =0.0009. mAb1[GluN2A] *VS* mAb3[GluN1]: P = 0.001. n = 9 for each group. Scale bar: 500µm for B, B', C, C', D, D'; 5µm for G.

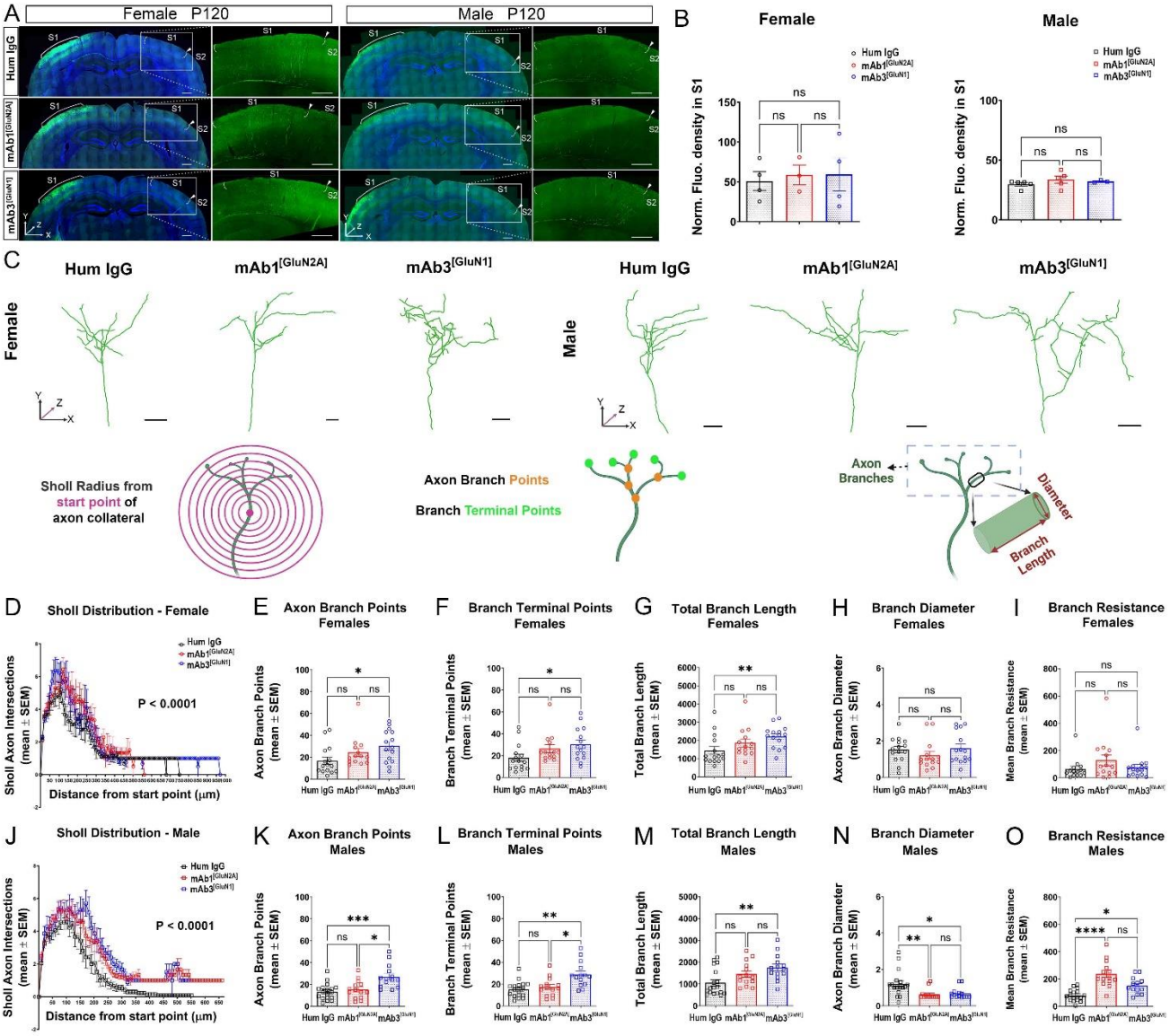

Figure 4: **Permanent morphological alterations of S1 callosal axons in mAb1[GluN2A] and mAb3[GluN1] treated mice.** (A) Disrupted callosal innervation pattern in S1 caused by injection of mAb1[GluN2A] and mAb3[GluN1] from P3 to P12 during development was recovered when mice were at P120. (B) Quantification of fluorescence density. Human IgG *VS* mAb1[GluN2A]: P > 0.999 (female); P = 0.50 (male). Human IgG *VS* mAb3[GluN1]: P > 0.999 (female); P = 0.87 (male). mAb1[GluN2A] *VS* mAb3[GluN1]: P > 0.999 (female); P > 0.999 (male). (C) Represented morphology of individual callosal axon terminals in S1 at P120. (D-O) Morphological features of axon branch terminals in mAb treated female (D-I) and male (J-O) mice. Sholl analysis of callosal axon branches in female (D) and male

(J) mice. Concentric circles from start point are used to count the numbers of axon intersections. Start point was defined at 10μm before the first branch intersection along the main axon trunk (magenta point in the diagram). Human IgG *VS* mAb1[GluN2A]: P = 0.0007 (female); P < 0.0001 (male). Human IgG *VS* mAb3[GluN1]: P > 0.999 (female); P < 0.0001 (male). mAb1[GluN2A] *VS* mAb3[GluN1]: P < 0.0001 (female); P = 0.065 (male). Comparison among three groups in axon branch points (E, K), branch terminal points (F, L), total branch length (G, M), branch diameter (H, N) and branch resistance (I, O). **P* < 0.05; ***P* < 0.05; ****P* < 0.01. n = 3 to 5 per group (B). n = 14 to 18 per group (D-O). Above statistics were based One-way ANOVA (Kruskal-Wallis Test).

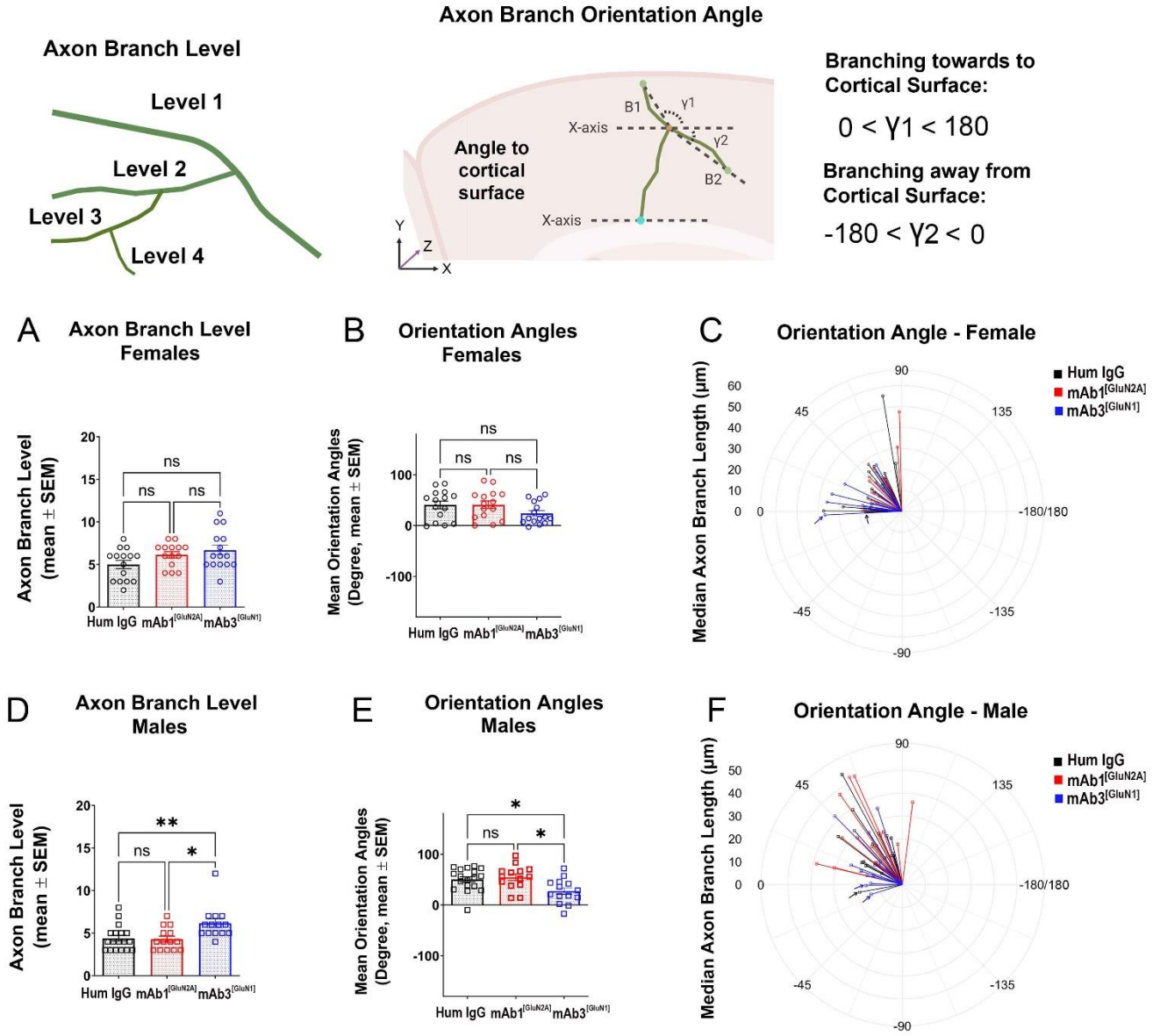

Figure 5: mAb3[GluN1] treated male mice displayed significantly increased axon branch levels and altered branch orientation angles. (A, D) Axon branch level. There was no difference in female mice (A), but

significantly increased branch level in mAb3[GluN1] treated male mice (D). Axon branch orientation angle in female (B, C) and male (E, F) mice. The angle forms between extending line connecting distal axon branch segment to x-axis of image within the XY plane. X-axis is parallel to the cortical surface. Angle is from -180 to 180 degree and is used to quantify the extending direction of axon branch to cortical surface. Positive angle (0 - 180) means axon branch is extending towards to cortical surface, while negative angle (-180 - 0) means axon branch is extending away from cortical surface. Arrows in C, F pointed the negative angles. *$P < 0.05$; **$P < 0.05$. n = 14 to 18 per group. Above statistics were based One-way ANOVA (Kruskal-Wallis Test).

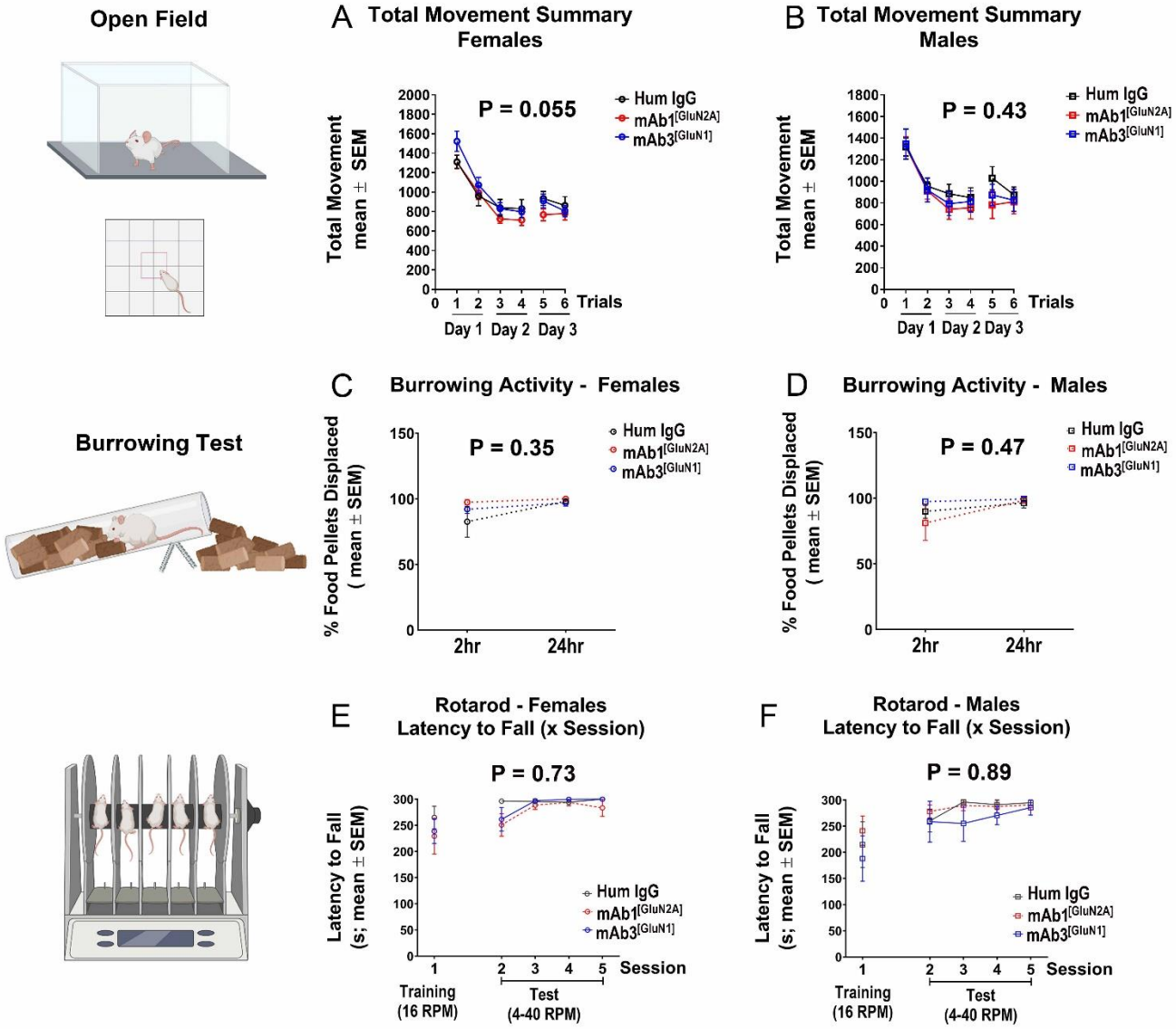

Figure 6: **Unaffected coarse movements in mAb1[GluN2A] and mAb3[GluN1] treated mice.** (A, B) Locomotor activity in Open Field Test (OFT). There was no difference of total movements among Human IgG, mAb1[GluN2A] and mAb3[GluN1] treated female (A) and male (B) mice. (C, D) Digging and kicking activity in burrowing test.

There was no difference of burrowing performance among the three groups of females (C) and males (D) mice. (E, F) Motor coordination in rotarod. There was no difference of rotarod performance among the three groups of females (E) and males (F) mice. n = 6 to 8 per group. Above statistics were based on Two-way ANOVA and Geisser-GreenHouse correction.

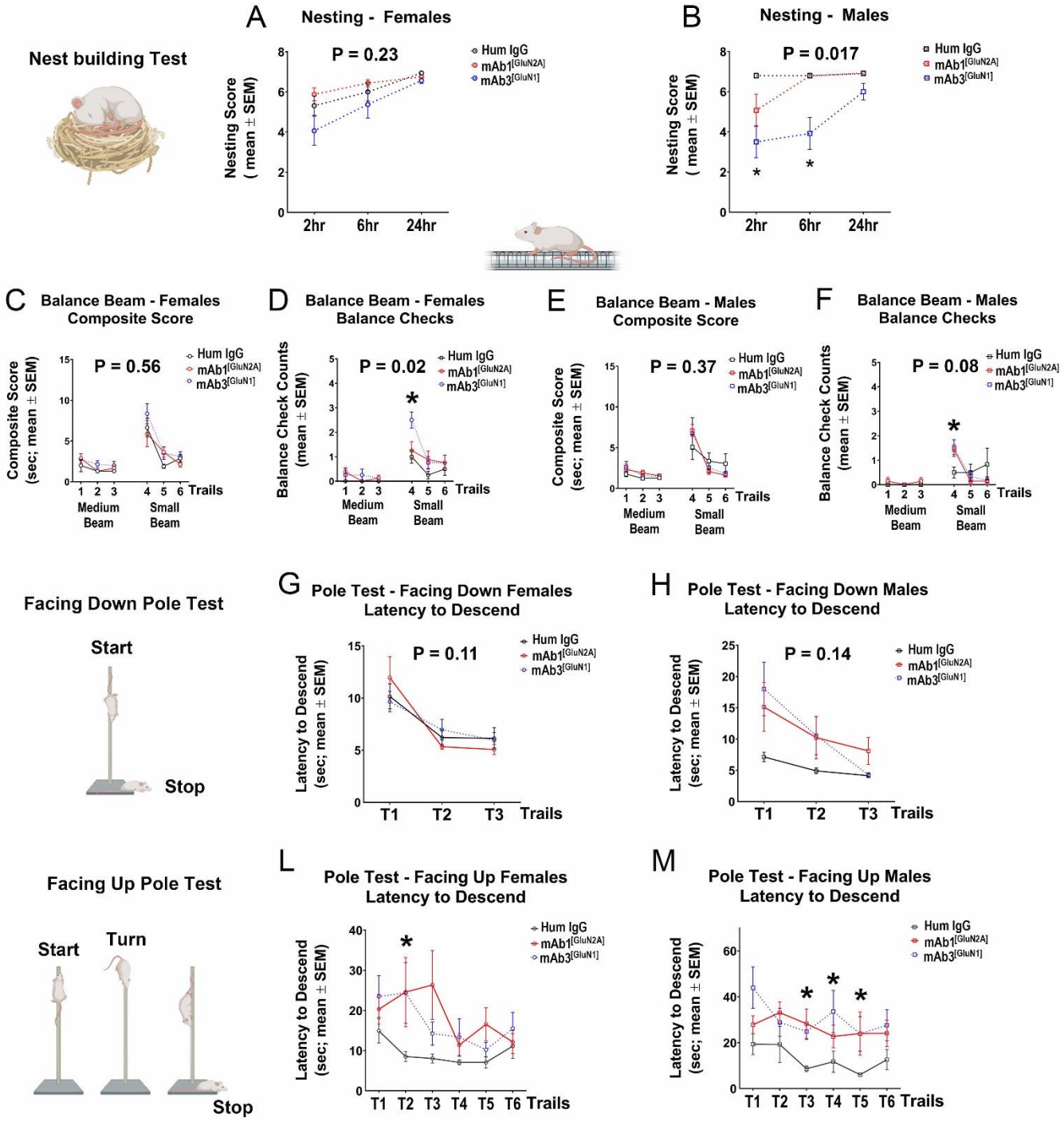

Figure 7: Persistent impaired fine movements in mAb1[GluN2A] and mAb3[GluN1] treated mice. (A, B) Nest building. There was significantly impaired nest building in mAb3[GluN1] treated male mice at 2hr (Human IgG *VS* mAb3[GluN1]: P = 0.02) and 6hr (Human IgG *VS* mAb3[GluN1]: P = 0.03) (B). (C-F) Balance beam. There was no difference in latency of beam crossing for female (C) and male (E) mice. However, there was significantly increased balance check in mAb3[GluN1] treated female mice (D) at trail 4 (Human IgG *VS* mAb3[GluN1]: P = 0.009) and mAb1[GluN2A] treated male mice (F) at trail 4 (Human IgG *VS* mAb1[GluN2A]: P = 0.03). (G, H) Facing down pole test. There was no difference in descent latency for female (G) and male (H) mice. (L, M) Facing up pole test. There was significantly increased descent latency in mAb3[GluN1] treated female mice (L) at trail 2 (Human IgG *VS* mAb3[GluN1]: P = 0.01), mAb1[GluN2A] treated male (H) at trail 3 (Human IgG *VS* mAb1[GluN2A]: P = 0.02), and mAb3[GluN1] treated male (H) at trail 3 (Human IgG *VS* mAb3[GluN1]: P = 0.04), trail 4 (Human IgG *VS* mAb3[GluN1]: P = 0.04), and trail 5 (Human IgG *VS* mAb3[GluN1]: P = 0.03). n = 6 to 8 per group. Above statistics were based on Two-way ANOVA and Geisser-GreenHouse correction or One-way ANOVA (Kruskal-Wallis Test) for each trial in L and M.

Table 1, Summary of morphological alterations in S1 callosal axons for mAbs treated mice.

Treatment	Gender	Branch Dimeter	Branch Numbers	Branch Levels	Branch Angle	Branch ORIEN	Total Branch Length	Terminal Field Area
mAb1[GluN2A]	**Female**	–	–	–	–	–	–	↑
mAb3[GluN1]	**Female**	–	↑	–	–	–	↑	–
mAb1[GluN2A]	**Male**	↓	–	–	–	–	–	↑
mAb3[GluN1]	**Male**	↓	↑	↑	↑	←→	↑	↑

–: No Change; ↓: Reduced; ↑: Increased; ←→: Opposite Direction

Table 2, Summary of impaired fine movements in mAbs treated mice. Locomotor activity, muscle strength, and muscle coordination served as controls for baseline movement activity.

Treatment	Gender	Locomotor Activity	Muscle Strength	Muscle Coordination	Nest Building	Balance Check	Latency of Facing Up Pole
mAb1[GluN2A]	**Female**	–	↑	–	–	–	–
mAb3[GluN1]	**Female**	–	–	–	–	↑	↑
mAb1[GluN2A]	**Male**	–	–	–	–	↑	↑
mAb3[GluN1]	**Male**	–	–	–	✖	–	↑

–: No Change; ↑: Increased; X: Impaired

Materials and methods

Experimental Model and Subject Details

All animal protocols were in accordance with the regulations of the National Institute of Health and approved by the University of California San Francisco Institutional Animal Care and Use Committee (IACUC). Floxed NR1 allele (Stock #005246), EMX1-Cre (Stock #005628) and Ai14 Cre reporter allele (Stock # 007914) were obtained from Jackson Laboratories (Bar Harbor, ME, USA). Wild-type CD1 mice were obtained from Charles River Laboratories. Male and female embryos at embryonic (E) 15.5 were used for the *in utero* electroporation, and pups between postnatal day 0 (P0) to 14 (P14) for the experiments.

***In utero* Electroporation:** DNA solution including the plasmid and 0.04% fast green was injected into the medial region of the lateral ventricle of the embryonic brain with a glass micropipette. Electrical pulses then were delivered to embryos by electrodes connected to a square-pulse generator (ECM830, BTX). For each electroporation, five 35-V pulses of 50ms were applied at 1s intervals. After the electroporation, the uterus was returned to the abdominal cavity, followed by suturing of the abdominal wall and skin. Mice were perfused at different postnatal stages using 4% paraformaldehyde followed by post-fixed overnight and incubation in 30% sucrose at 4°C. 35 μm-thick coronal sections were obtained using cryostat sectioning.

Plasmid: The ubiquitin-EGFP plasmid used was from a previous study (16).

Antibodies: Antibodies for intraventricular injection: Patient derived monoclonal anti-NMDAR antibodies were made by Ariele Greenfield and Rita Loudermilk in Michael Wilson's lab (For details see **Methods for making monoclonal antibody from anti-NMDAR encephalitis patient**). Human IgG (#009-000-003, Jackson ImmunoResearch) served as control. **Antibodies for immunostaining**: goat anti-EphB2 (1:50, AF467, R&D), anti-human 488 (#109-545-088, Jackson ImmunoResearch), donkey anti-goat cy3 (#705-165-003, Jackson ImmunoResearch). **Antibodies for immunoprecipitation:** human IgG (#009-000-003, Jackson ImmunoResearch), CSF from patient without anti-NMDAR encephalitis patient (neuropsychiatric lupus), CSF of anti-NMDAR encephalitis patient, monoclonal antibodies (18-20ug/ml for immunostaining) mAb1, mAb2, mAb3, mAb4 made from the anti-NMDAR encephalitis patient. **Antibodies for western blot**: rabbit anti-NR1 (AB9864, Millipore), IRDye 800CW Goat x Rabbit IgG(H+L) Ab (1:20000, #925-32211, Li-Cor).

Methods for Making Monoclonal Antibody from anti-NMDAR Encephalitis Patient

Patient Recruitment and Eligibility Criteria

Inclusion criteria for this study was enrollment in "Immunological Studies in Multiple Sclerosis, Neuromyelitis optica, Sarcoidosis, or Immune Mediated Central Nervous System Disorders" and diagnosis of antibody-positive

NMDA receptor encephalitis. The patient consented to donating CSF and blood, and patient demographics and clinical history were obtained as part of the above study. All studies were approved by the UCSF Institutional Review Board.

Patient Cerebrospinal Fluid Collection, Processing and Fluorescence-activated cell sorting (FACS)

12 ml of fresh CSF was centrifuged at 400g x 15 minutes at 4°C to separate a cell pellet from supernatant. Supernatant was removed immediately to avoid cell dispersion, and care was taken to minimally move the source 15ml conical tube. Wide bore pipette tips were used when handling cells to preserve cell integrity.

Destination FACS tubes (1.5ml Eppendorf) were coated overnight with 100% FBS to minimize cell adhesion. Destination tubes were filled with 450µl of cold D-PBS + 15% FBS and placed lid-open in front of a de-static bar prior to placing them in the cell sorter. Cell samples were blocked with FcR Block (Miltenyi Biotec) and stained with fluorescent antibodies to cell surface markers: IgD Brilliant Violet 421 (Biolegend 11-26c.2a), CD20 FITC (Beckman Coulter B9E9), CD38 PerCPCy5.5 (BioLegend HIT2), CD3 PE-Cy7 (Beckman UCHT1), CD138 PE (Miltenyi 449), CD27 APC (eBioscience O323), CD19 APC-Alexa750 (Beckman J3-119). CSF B cell subsets were sorted on a Beckman MoFlo Astrios FACS sorter as previously described (51). CD27hi plasmablast/plasma cells (CD27hiPC: CD19+IgD-CD27hi), the vast majority of which are also CD38+, were then used for single cell printing.

Single Cell Printing of FACS-sorted CSF cells

$CD27^{hi}$PC cell suspensions were diluted to a 5% FBS concentration immediately prior to being centrifuged at 300g x 5min at 4°C. Pelleted cells were gently resuspended in 5-20µl of supernatant then placed on ice in a vacuum chamber for 5min. A ~5µl droplet of cells was pipetted onto a hydrophobic slide and aspirated for single cell printing by the CellenONE/sciDROP PICO system (Cellenion, Lyon, France and SCIENION, Berlin, Germany). Single cells were detected by the CellenONE and dispensed into wells of a 384-well PCR plate filled with 2µl/well of lysis buffer as described in the Smart-seq2 protocol (52).

Single cell immune repertoire sequencing and monoclonal antibody production

Cell-containing PCR plates were briefly vortexed and centrifuged at 2000 rpm x 1 minute, placed on dry ice and immediately stored at -80°C. We then performed RT-PCR using template switching and total cDNA amplification and bead clean as previously described (52). This was followed by targeted PCR of the heavy and light chains using primers to the leader sequences and constant region 1, followed by nested PCR as previously described (53). Products were sequenced via Sanger sequencing. Mapping of germline V, D, J and CDR3 regions was performed using IgBlast and IMGT V-Quest. Alignments were generated in Geneious (Biomatters). Recombinant monoclonal antibodies were produced with a high throughput method using a mammalian cell line (Tuna293) at

LakePharma (San Carlos, CA), with mass spectrometry validation that the monoclonal antibody amino acid sequence matched the patient-derived Sanger sequence.

Hippocampal Neuronal Cultures: Hippocampi from male and female *Emx1*$^{cre/+}$; *NR1*$^{fl/fl}$; *Ai14*$^{fl/fl}$ and littermate *Emx1*$^{cre/+}$; *NR1*$^{wt/wt}$; *Ai14*$^{fl/fl}$ mice were dissected at P0-P1 and incubated with trypsin at 37° C for 15 min. Cells were then dissociated by trituration with fire-polished Pasteur pipettes. Neurons were plated on poly-D-lysine (Sigma-Aldrich) and mouse laminin (Invitrogen) coated 12 mm glass coverslips (Warner Instruments) at $5x10^4$ cells per well in a 24-well plate in plating media (minimal essential medium [MEM], 10% FBS, 0.5% glucose, 1 mM sodium pyruvate, 25 µM glutamine, and 50 units penicillin/streptomycin). After 4 h, medium was changed to Neurobasal medium supplemented with B-27 (Gibco), GlutaMAX (Gibco), and 50 units pen/strep (Gibco). Cultures were maintained in an incubator with 5% CO2 at 37°C, and half of the medium was replaced as needed.

Live Neuron Staining: At DIV 21, neurons were incubated with in-house monoclonal antibodies for 2 hours at 37°C. Following incubation, neurons were washed with warmed PBS and fixed with ice-cold 4% PFA in 0.1 M Na-acetate, pH 6.0 for 20 min at 4°C and washed thoroughly with PBS. Neuron-plated coverslips were blocked in 10% serum, 0.1% Triton-X-100 for 2 hours at room temperature. Primary antibodies were probed with donkey-anti-human Alexa Fluor 488 (Invitrogen) for 2 hours at room temperature and mounted in Prolong Gold (Invitrogen). Images were acquired using a Nikon Ti microscope equipped with an Andor Borealis CSU-W1 spinning disk confocal and Andor Zyla sCMOS camera (Nikon Core UCSF).

Intraventricular Injection: Antibodies were injected to lateral ventricular of pups by glass pipette with a sharp bevel at 45 degrees (BV-10 Micropipette Beveler, Sutter instrument). The diameter of pipette tip was ~40-80µm (54). The concentrations for antibody injections were 2.0µg/µl for mAbs and Hum IgG. Antibodies were injected twice-daily, and the injection volume was 0.8-1µl for each injection.

Slice Preparation and Imaging: Mice were perfused with saline followed by 4% paraformaldehyde in phosphate buffered saline (PBS), pH7.4. Brains were removed from mice and post-fixed in 4% paraformaldehyde overnight before being placed in 30% sucrose solution. The brains were then cut into 12-µm, 35-µm and 200-µm sections with cryostat (Leica VT1200S). Sections were imaged by Zeiss Axioscan Z.1 (Zeiss, Thornwood, NY, USA) with a 20X objective. Confocal images were taken by Zeiss LSM880 (Zeiss, Thornwood, NY, USA) with 20X objective, 63X oil objective and 100X oil objective.

Immunostaining: Mice were perfused with saline followed by 4% paraformaldehyde in phosphate buffered saline (PBS), pH7.4. Brains were removed from mice and post-fixed in 4% paraformaldehyde overnight before being placed in 30% sucrose solution. The brains were then cut into 12-µm sections with cryostat (Leica VT1200S). Non-specific binding was blocked by adding 5% normal goat/donkey serum during pre-incubation and incubations in 1x PBS containing 0.05% TritonX-100. The primary antibodies were applied overnight at 4 degrees. Secondary

antibodies were applied for 1-2 hours at 4 degree and nuclei were stained with DAPI. Slides were mounted with Prolong Gold Anti-fade Mountant (P36930, Invitrogen).

Immunoprecipitation (IP): Adult mice at P40 were used for immunoprecipitation. **A single** mouse brain was homogenized in homogenizing buffer (1% Triton X-100, 150 mM NaCl, 50 mM Tris-HCl pH 7.5, 2 cOmplete protease inhibitor tablets (Roche), 1 phosSTOP phosphatase inhibitor tablet (Roche)) with Dounce homogenizer on ice. The lysate was then centrifuged at 10,000g for 10 min at 4°C. For each IP, 300μl of supernatant was transferred into a labelled IP tube and 700 μl of lysis buffer was added to achieve ~2 μg/ μl brain lysate. 30μg monoclonal antibody (mAb) or ChromoPure IgG control (Sigma) was added to each IP tube and mixed by rotator for 4hr at 4°C. Then, 50uL of equilibrated magnetic protein A/G beads (Thermo Scientific) were added to each IP reaction and mixed by rotator for 1hr at 4°C. Afterward, beads were washed with cold lysis buffer three times. At last, 50 μl sample buffer was added to beads to elute the protein and the IP elution was then subjected to western blotting by SDS-PAGE of IP eluates on a 4-12% Bis-Tris gel.

Quantification and Statistical Analysis

Callosal Axon Density Analysis: Sections were imaged by Zeiss Axioscan Z.1 (Zeiss, Thornwood, NY, USA) with 20X objective over whole brain section. Each image was made up by the compression of three slices in 4μm Z-stack. For each brain, only one section was chosen for data quantification. The callosal axon density (fluorescence density) in S1 was quantitatively analyzed by ImageJ software. See the details in Zhou et al., (8)

Individual axon terminal tracing: 200-μm coronal section of P120 mouse brain were imaged by Zeiss LSM880 (Zeiss, Thornwood, NY, USA) with 20X objective. 3D confocal image of S1 callosal axon terminals loaded in Imaris 9.8 (Oxford Instruments). The morphology of individual callosal axon terminals was tracked manually with combining Autopath function in Imaris. All calculations on traced callosal axon terminals were automatically done by Imaris.

Mouse Behavioral Tests

All mouse behavioral tests were runed in Gladstone Behavioral Core. The use and care of the mice complied with the guidelines of the Institutional Animal Care and Use Committee of UCSF. All animals were maintained in 12 hr light/dark schedule and with access to food and water, ad libitum. Before behavioral testing, mice were transferred to the testing room and acclimated for at least 1 hour. All work surfaces were cleaned with Vimoba (100 ppm chlorine dioxide solution made from MB-10 Tablets, Quip Laboratories) before and after testing every day and with 70% alcohol between testing of different mice.

Elevated Plus Maze Test

Elevated plus maze is used to evaluate anxiety-related behavior. The maze consists of two open and two enclosed arms elevated 63 cm above the ground (Hamilton-Kinder, Poway, CA). Mice are placed at the intersection between the open and closed arms and allowed to explore for 10 min. Anxiety-related behavior was measured by the time and distance traveled in the open arm.

Open Field Test

Open field test is used to measure locomotion and anxiety-related behavior. Mice are placed in the center area of open field chamber (16 in x 16 in) with dim light in the dark phase for 10 min. Mice trajectory was recorded with photobeam assays (San Diego Instrument, San Diego, CA). Center area is an 8 in x eight in square in the center part of the chamber. Anxiety-related behavior was defined by ratio of traveled in the center area to total area. Total movements, rearing in the open field, and time spent in the center and periphery of the open field were recorded automatically for subsequent analysis.

Nest Building Behavior Test

Nest building is spontaneous home cage behavior of mice. For assessment of nest building behavior, group-housed mice were transferred individually to new cages. A 5 × 5-cm white compressed cotton pad (Nestlets, Ancare) was placed in the center of the cage, and nest building behavior was assessed 2, 6, and 24 hours later. Composite nest building scores were assigned at each time point as follows: 0, nestlet untouched; 1, < 10% of nestlet shredded; 2, 10%–50% of nestlet shredded but nest was without shape; 3, 10%–50% of nestlet shredded and nest had shape; 4, 50%–90% of nestlet shredded but nest was without shape; 5, 50%–90% of nestlet shredded and nest had shape; 6, > 90% of nestlet shredded but nest was flat; and 7, > 90% of nestlet as shredded and nest had walls that were at least as tall as the mouse on > 50% of its sides.

Burrowing Behavior Test

Burring behavior is used to evaluate spontaneous home cage behavior of mice. A burrow is made of 200 mm long, 68 mm diameter tube. The open end of the tube is raised 30 mm by bolting two 50 mm machine screws through it, each 10 mm in from the end. The lower end of the tube is closed with a plug. Fill the burrow with 200 g food pellets for mice and place the burrow against the longer wall of a clean cage with a thin layer of bedding. The closed end of the burrow is against the back wall of the cage. Provide water but no extra food in the cage hopper for the mice. Test is started 3hr before dark cycle. The displaced food pellets in the burrow were measured at 2hr and 24hr after cage-burrow setup.

Rotarod Test

Rotarod is used to evaluate motor coordination of mice. Rotarod was performed with a Med Associates ENV-575(M) apparatus, using a 3-day protocol. Day 1 involved three training runs at fixed 16 rpm. Days 2 and 3 each

involved 6 data runs, 3 in the morning and 3 in the afternoon. The data runs on days 2 and 3 used steady acceleration of the rod from 4-40 rpm over 5 min. The time was stopped at 5 min or when the mouse fell. Photobeams were interrupted by the experimenter if the mouse held onto the rod without walking for three full rotations. Each mouse was given three trials at least with a 15-min inter-trial interval and a maximum of 300 s per trial. The average latency to fall off the Rotarod was calculated.

Balance Beam Test

Balance beam is used to evaluate motor coordination and balance. A 15" long plastic beam is suspended about 20" above the table, with an open platform at one end and a dark box with 1.5" square opening at the other end. Balance beam test was taken place over 3 days with 3 trials per day. The first day included two additional training trials. On the first training trial of the first day, mice were placed on the middle of the largest diameter beam facing a dark box and guided to the enclosure. On the second training trial on the first day, mice were placed on the end of the beam facing the dark box and guided to the enclosure. On the third to fifth trials (testing trials) on the first day, mice were placed on the end of the beam facing the dark box and traversed the beam unguided. On the second day, mice were placed at the end of the medium diameter beam, facing the dark box. On the third day, mice were placed at the end of the smallest diameter beam, facing the dark box. Latency to traverse the beam into the dark box, number of foot slips, and the number of falls were recorded. Trials were limited to a maximum latency of 60s.

Pole Test

The pole test evaluates the ability of the mouse to grasp and maneuver on a pole in order to descend to its home cage. The vertical pole is 50 cm long (1 cm diameter) with rough surface. The base of the pole was placed in the home cage. Pole test was taken place over 2 days. The first day included three facing down training trails and three facing up testing trials. The second day included three facing up testing trails. In the training trails, mice were placed facing down atop of the pole and the time to descend the pole was measured. In the testing trails, mice were placed upward atop of the pole. The latency for mice to turn around and climb down was recorded. Any slips or falls in both training and testing trails were also recorded. If a mouse falls at the beginning of the trial due to placement issues, mouse is replaced, and trial is restarted.

Grip Strength Test

The Grip Strength test is a complement to behavioral tests for motor coordination and motor function. The Grip-Strength Meter (Ugo Basile) was used to measure the grip strength on forelimbs and all limbs. Mice were placed over a base plate, in front of a grasping bar (either trapeze-shaped or the grid), whose height is adjustable. The grasping tool is fitted to a force sensor connected to the Peak Amplifier, which guarantees a reliable and

automated detection of the animal response. The force transducer has a maximum applicable force of 1500g, with a resolution 0.1g.

Inverted Grid Hang Test

The inverted grid hang test is used to measure the ability of mice to exhibit sustained limb tension to oppose their gravitational force. The apparatus consists of a 15x25 cm grid of fine wire mesh suspended 34 cm above the table on supports. The walls and rear of the supports are covered with smooth plastic boards to prevent escape, and a larger plastic board is placed atop the wire mesh to prevent a mouse from climbing around the edge. The tabletop was covered with layers of soft towels to prevent injury from a fall. Mice were placed on the wire mesh, gently shaken to ensure a grip, and the mesh then inverted onto the supports. Latency to fall was recorded within 180 s. Measurements were repeated three times.

Supplemental information

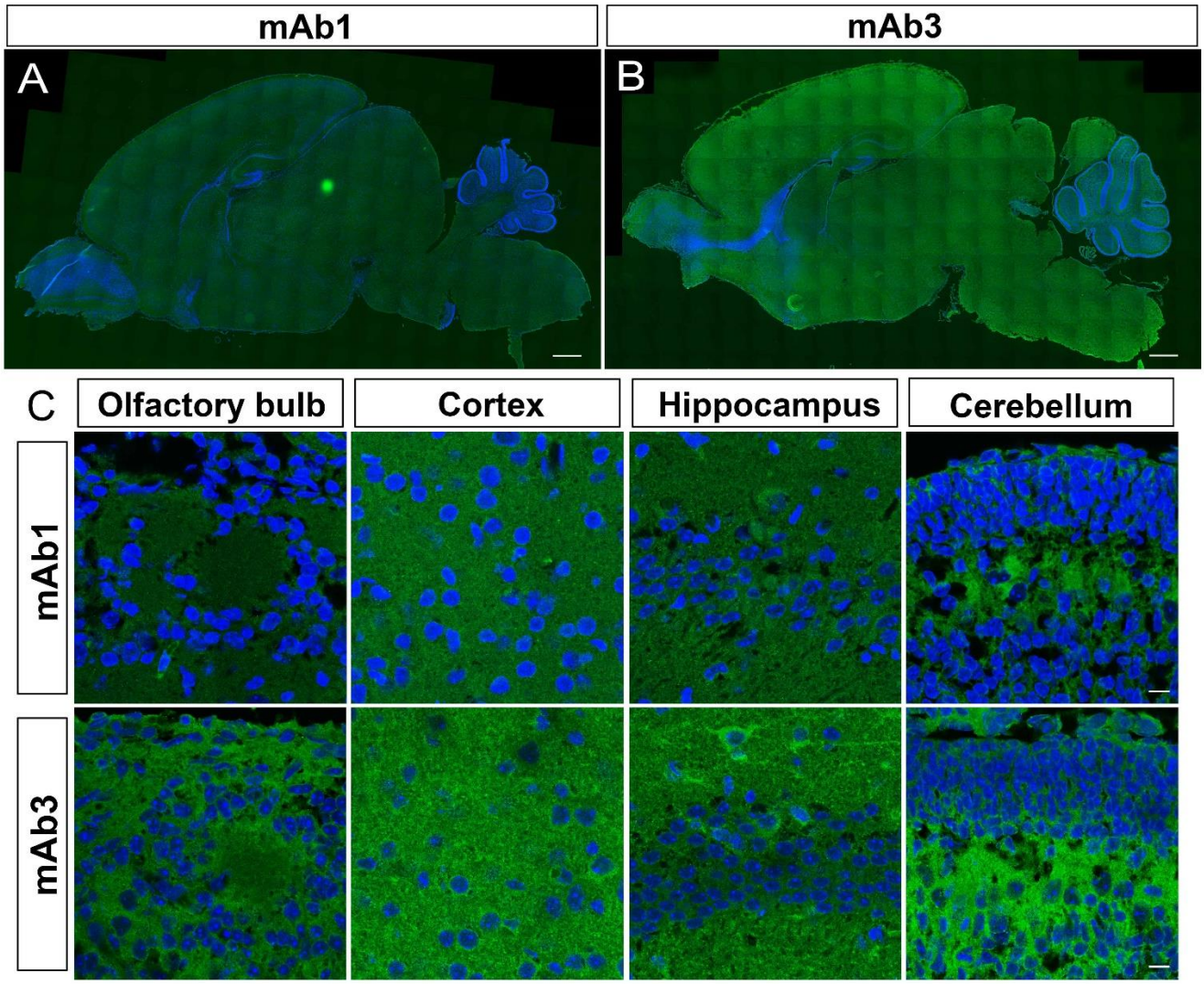

Supplementary Figure 1: Immunostaining pattern of mAb1 and mAb3 at early developmental stage. The immunostaining pattern mAb1 (A) and mAb3 (B) on sagittal sections of P8 mouse brains. (C) Immunostaining pattern of mAb1 and mAb3 in different brain regions. Scale bar: 500µm for images A, and B; 10µm for images in C.

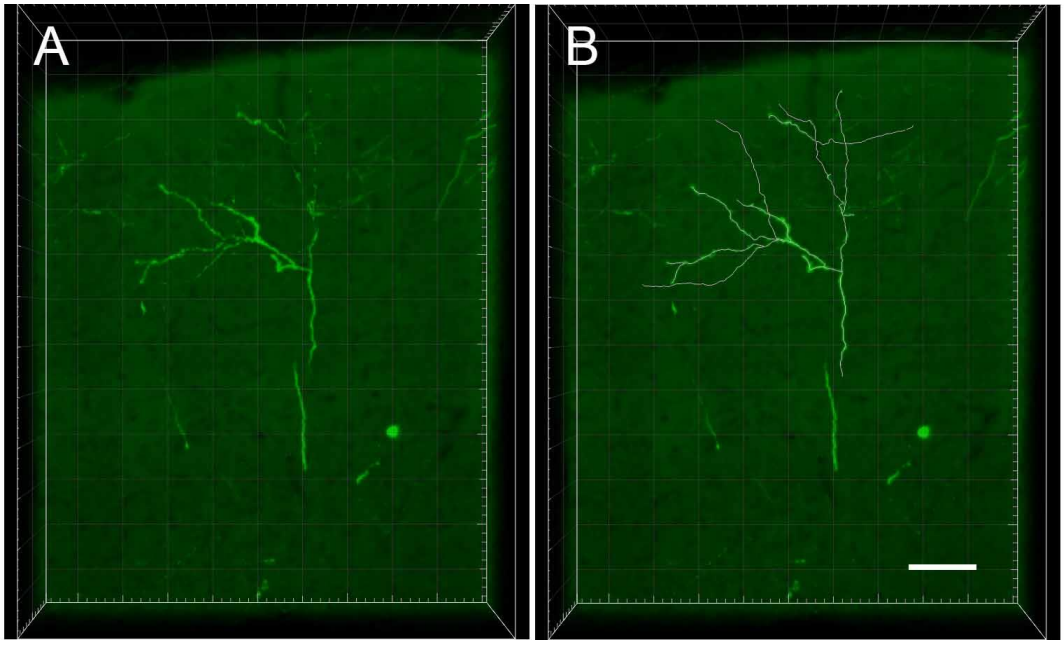

Supplementary Figure 2: Axon branches were traced semi-automatically using Imaris software. (A) 3D confocal image of S1 callosal axon terminals loaded in Imaris. Image was taken from a 200-µm coronal section of P120 mouse brain. (B) The morphology of individual callosal axon terminals was tracked across 3D in Imaris. Traced axon branches in Imaris. The morphology was tracked manually with combining Autopath function in Imaris. Scale bar: 70µm.

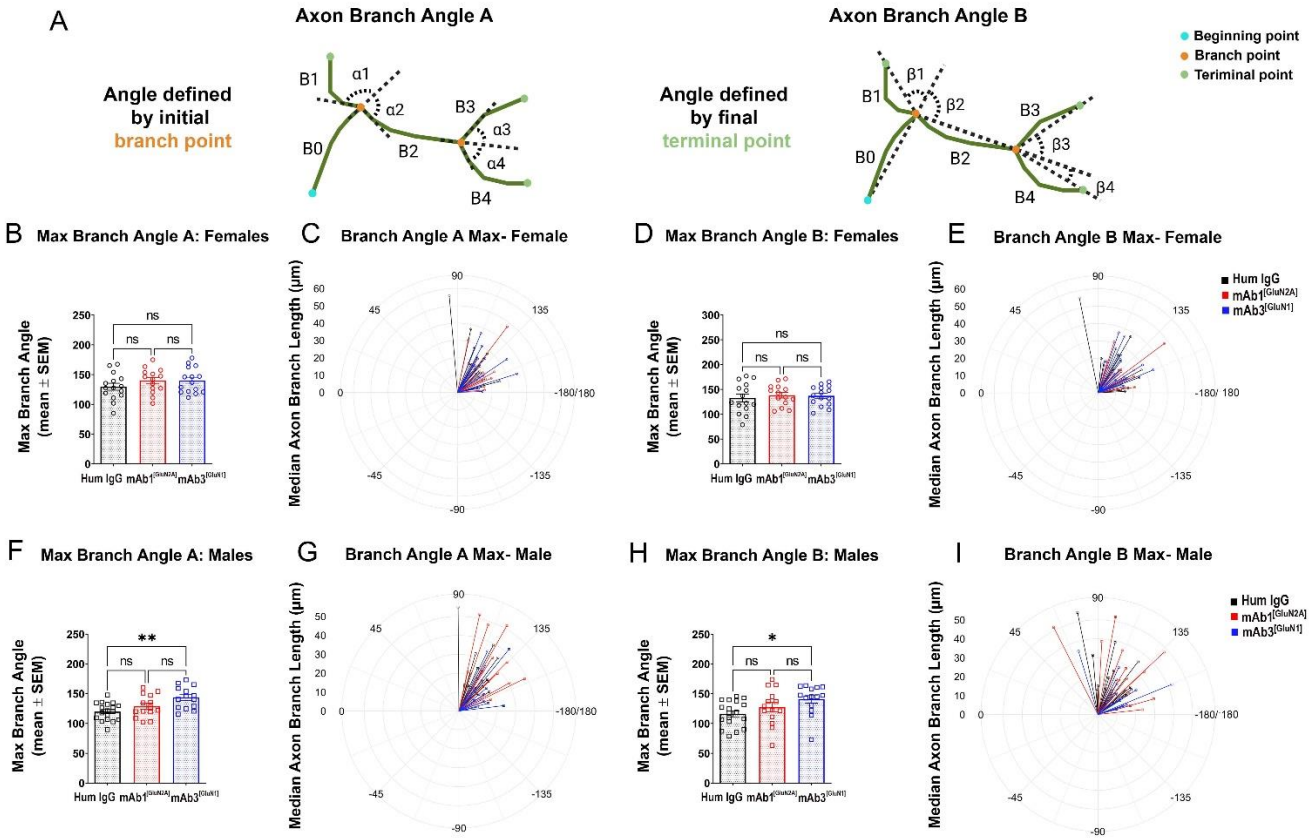

Supplementary Figure 3: Significantly increased branch angles in mAb3[GluN1] treated male mice. (A) Diagram of two ways to measure axon branch angles. Axon branch angle A: defined as the angle between the extending lines from the branch point and its peripheral neighbor vertex. Axon branch angle B: defined as the angle between the extending lines connecting the branch point with the neighboring branch points and the terminal points, respectively. Max branch angle A in female (B, C) and male (F, G) mice. Max branch angle B in female (D, E) and male (H, I) mice. *$P < 0.05$; **$P < 0.05$. n = 14 to 18 per group. Above statistics were based One-way ANOVA (Kruskal-Wallis Test).

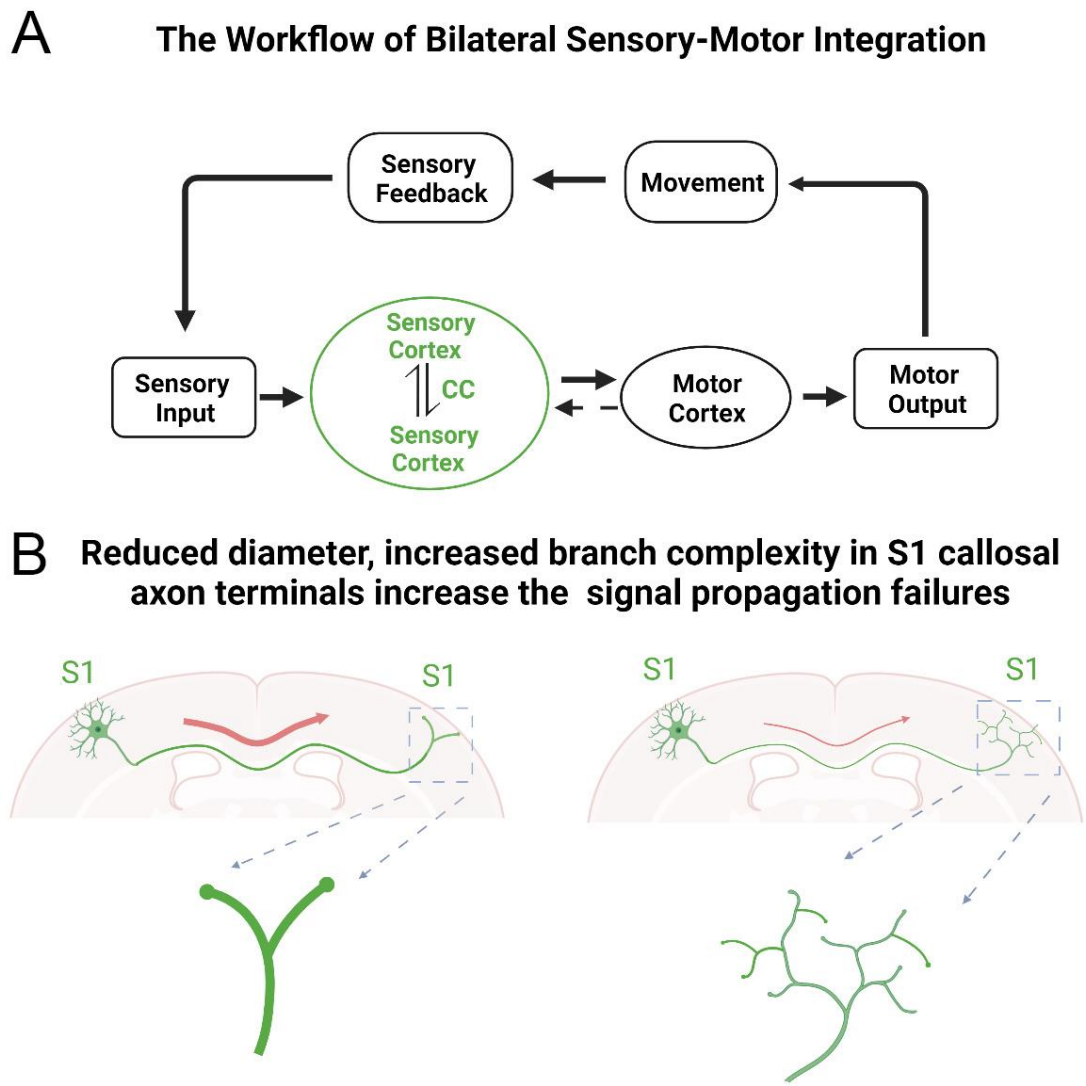

Supplementary Figure 4: Model of sensory-motor integration in somatosensory cortex. (A) Workflow of bilateral sensory-motor integration. (B) Model of morphometric features of callosal axons on sensory signal propagation in somatosensory cortex.

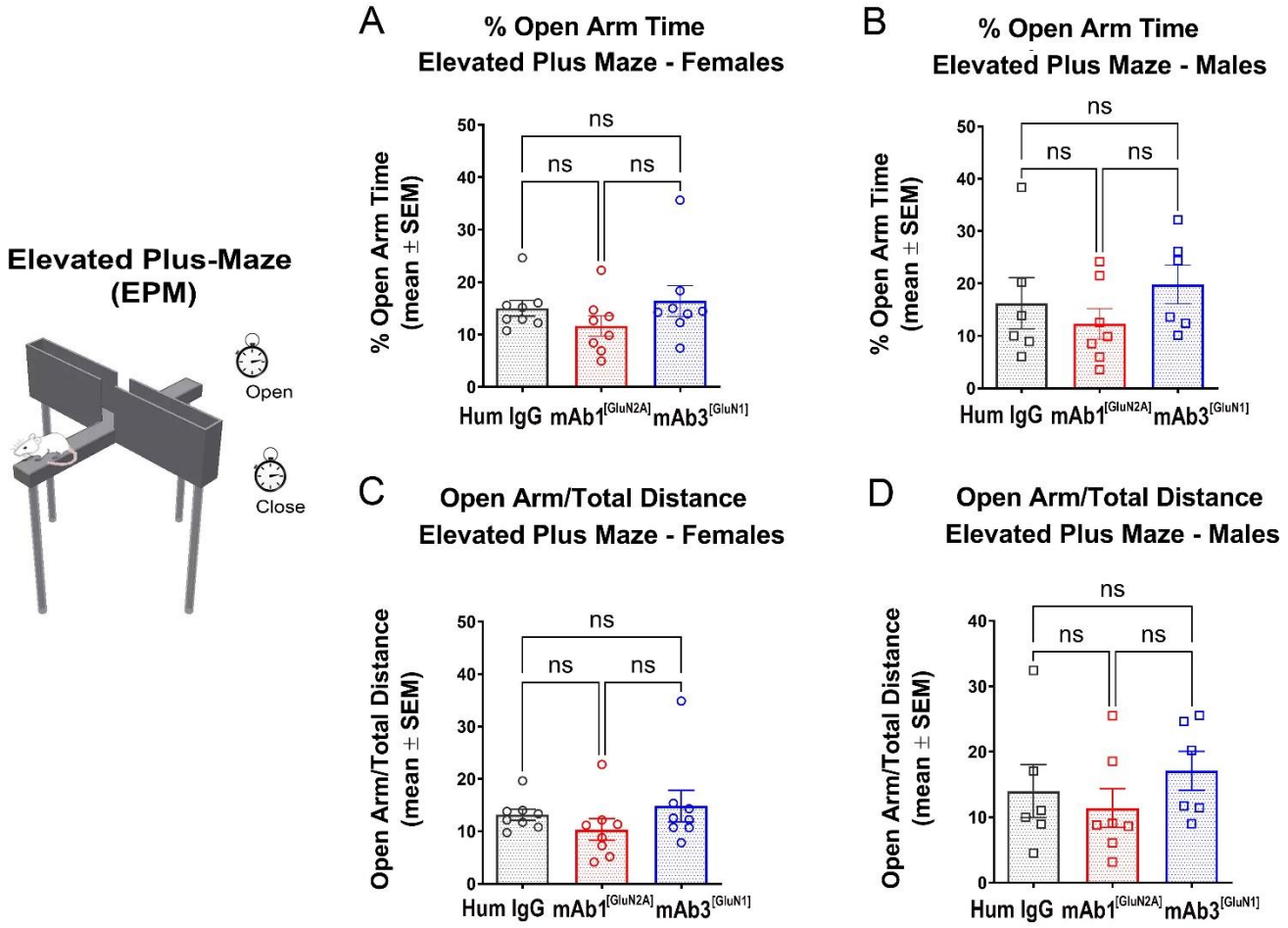

Supplementary Figure 5: No increased anxiety in mAb1[GluN2A] and mAb3[GluN1] treated mice. (A, B) Time traveled in the open arm of Elevated Plus-Maze (EPM). There was no difference of time spending on the open arms among Human IgG, mAb1[GluN2A], and mAb3[GluN1] treated female (A, P = 0.21) and male (B, P = 0.19) mice. (C, D) Distance traveled in the open arm of EPM. There was no difference of distance traveled on the open arms among Human IgG, mAb1[GluN2A], and mAb3[GluN1] treated female (A, P = 0.16) and male (B, P = 0.19) mice. n = 6 to 8 per group. Statistics were based on One-way ANOVA (Kruskal-Wallis Test).

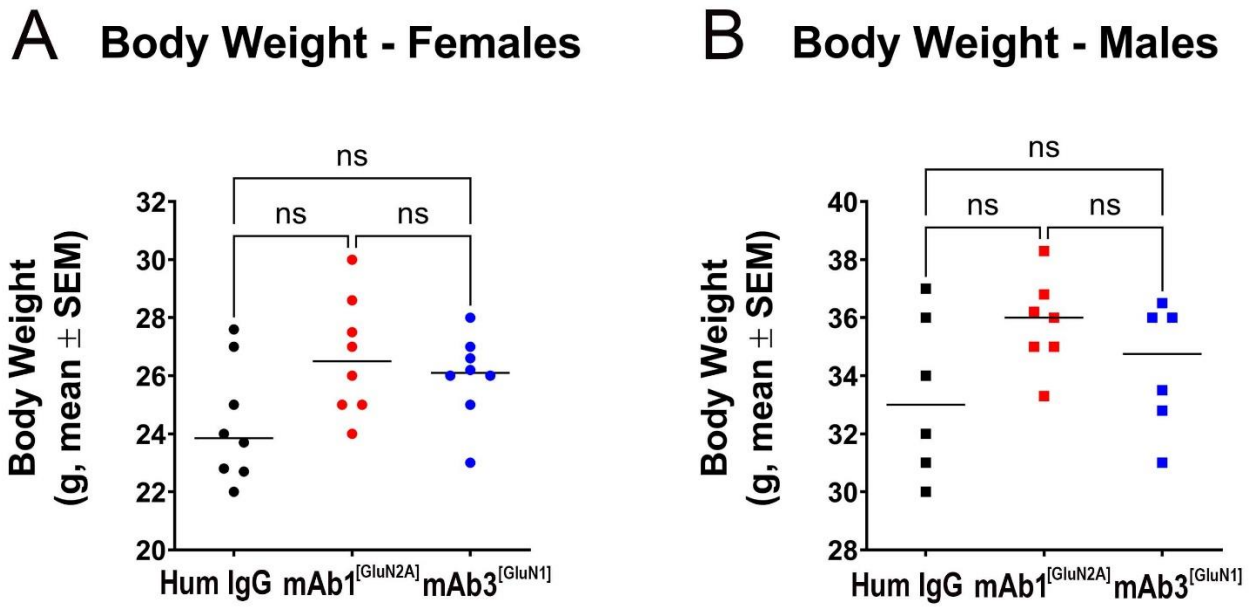

Supplementary Figure 6: No body weight difference among groups. (A) Comparison of body weight in female mice. Human IgG *VS* mAb1[GluN2A]: P =0.12. Human IgG *VS* mAb3[GluN1]: P =0.34. mAb1[GluN2A]*VS* mAb3[GluN1]: P > 0.999. (B) Comparison of body weight in male mice. Human IgG *VS* mAb1[GluN2A]: P =0.33. Human IgG *VS* mAb3[GluN1]: P > 0.999. mAb1[GluN2A]*VS* mAb3[GluN1]: P =0.83. n = 6 to 8 per group. Statistics were based on One-way ANOVA (Kruskal-Wallis Test).

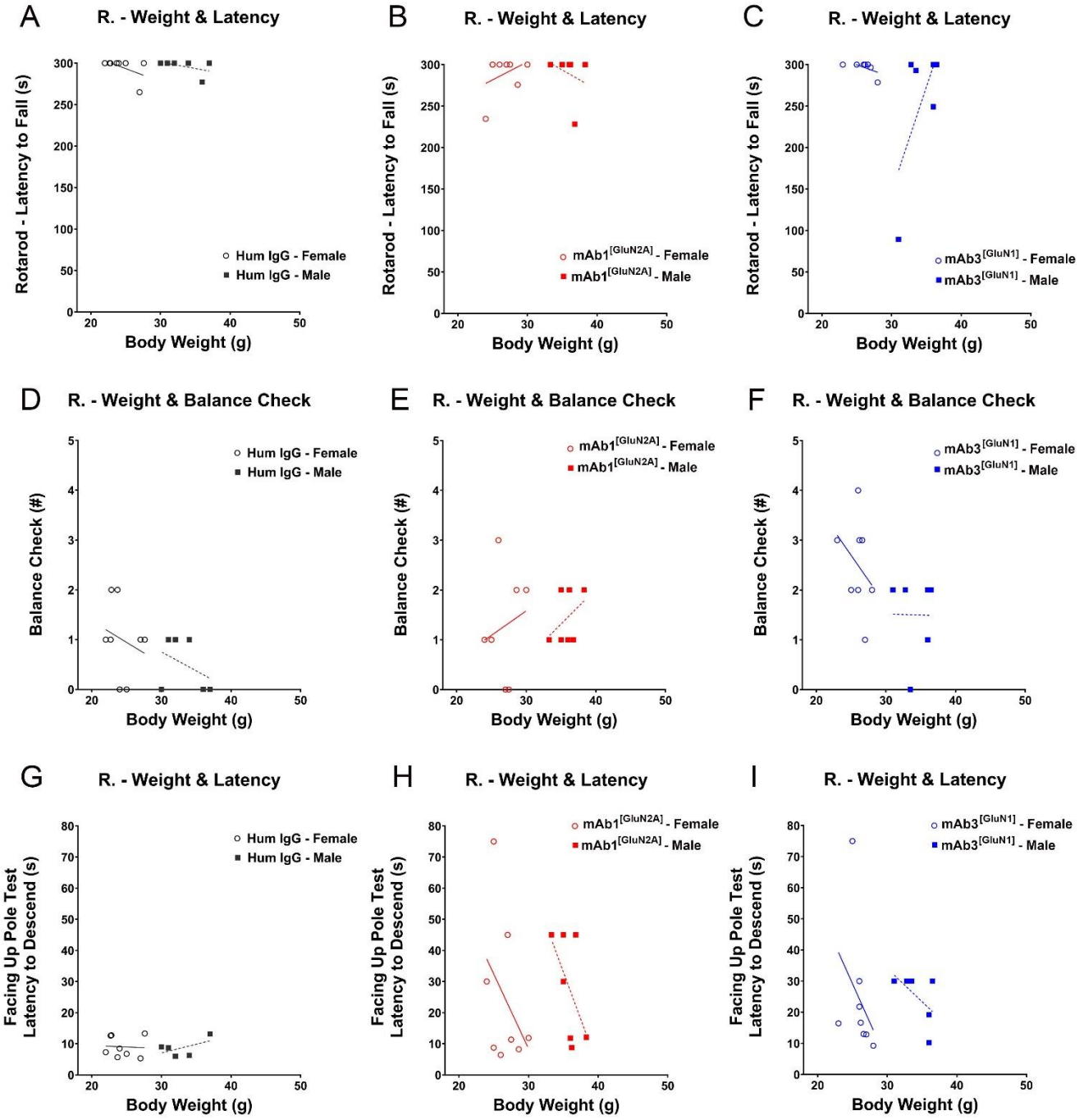

Supplementary Figure 7: No correlation between body weight and motor performance. (A-C) Correlation between weight and Latency to fall (session 2 of rotarod). (A) Human IgG (Female: $R^2 = 0.27$, P = 0.18 by linear regression; Male: $R^2 = 0.22$, P = 0.35). (B) mAb1[GluN2A] (Female: $R^2 = 0.14$, P = 0.36; Male: $R^2 = 0.08$, P = 0.54). (C) mAb3[GluN1] (Female: $R^2 = 0.36$, P = 0.11; Male: $R^2 = 0.44$, P = 0.15). (D-F) Correlation between weight and balance check (trail 4 of balance beam). (D) Human IgG (Female: $R^2 = 0.05$, P = 0.58; Male: $R^2 = 0.15$, P = 0.44). (E) mAb1[GluN2A] (Female: $R^2 = 0.04$, P = 0.65; Male: $R^2 = 0.17$, P = 0.36). (F) mAb3[GluN1] (Female: $R^2 = 0.10$, P =

0.44; Male: R^2 = 0.0001, P = 0.98). (G-I) Correlation between weight and Latency to descend (trail 2 of facing up pole). (G) Human IgG (Female: R^2 = 0.003, P = 0.90; Male: R^2 = 0.29, P = 0.35). (H) mAb1$^{[GluN2A]}$ (Female: R^2 = 0.16, P = 0.33; Male: R^2 = 0.32, P = 0.19). (I) mAb3$^{[GluN1]}$ (Female: R^2 = 0.12, P = 0.40; Male: R^2 = 0.31, P = 0.25).

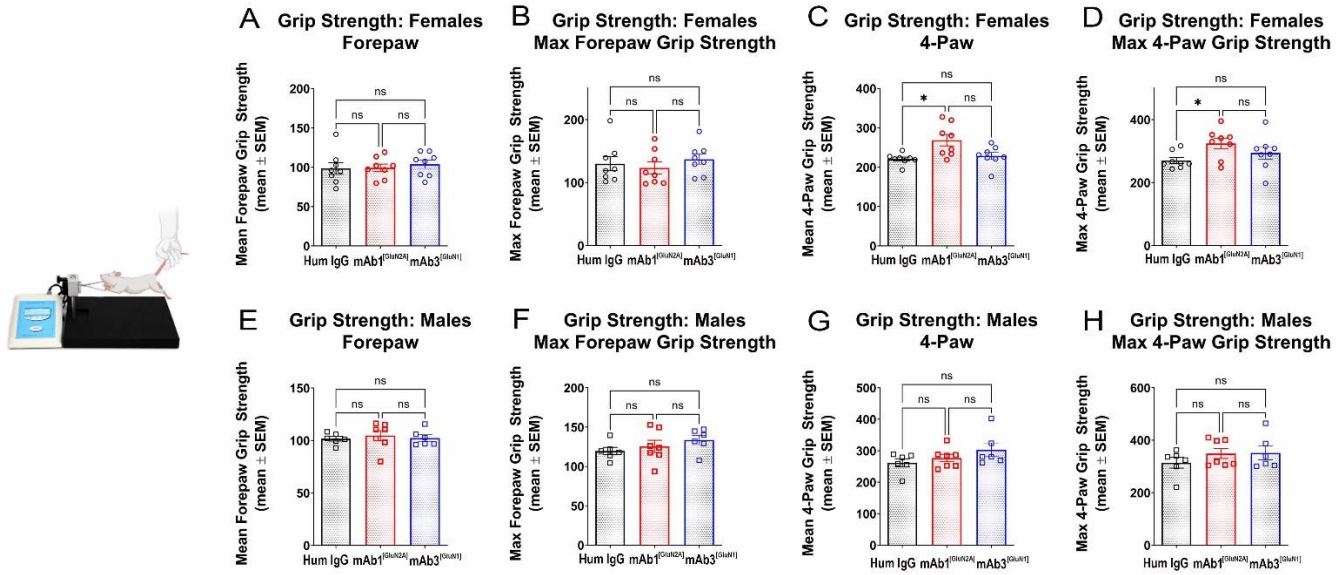

Supplementary Figure 8: No impaired muscle strength in mAb1$^{[GluN2A]}$ and mAb3$^{[GluN1]}$ treated mice. (A-D) Grip strength female mice. Human IgG served as controls. (A) No difference of mean forepaw grip strength in female mice. Human IgG *VS* mAb1$^{[GluN2A]}$: P > 0.999. Human IgG *VS* mAb3$^{[GluN1]}$: P =0.64. (B) No difference of max forepaw grip strength in female mice. Human IgG *VS* mAb1$^{[GluN2A]}$: P > 0.999. Human IgG *VS* mAb3$^{[GluN1]}$: P =0.96. (C) Significantly increased mean 4-paw grip strength in mAb1$^{[GluN2A]}$ treated mice. Human IgG *VS* mAb1$^{[GluN2A]}$: P = 0.008. Human IgG *VS* mAb3$^{[GluN1]}$: P =0.41. (D) Significantly increased max 4-paw grip strength in mAb1$^{[GluN2A]}$ treated mice. Human IgG *VS* mAb1$^{[GluN2A]}$: P = 0.03. Human IgG *VS* mAb3$^{[GluN1]}$: P =0.58. (E-H) Grip strength male mice. (E) No difference of mean forepaw grip strength in male mice. Human IgG *VS* mAb1$^{[GluN2A]}$: P =0.72. Human IgG *VS* mAb3$^{[GluN1]}$: P > 0.999. (F) No difference of max forepaw grip strength in female mice. Human IgG *VS* mAb1$^{[GluN2A]}$: P = 0.79. Human IgG *VS* mAb3$^{[GluN1]}$: P = 0.20.

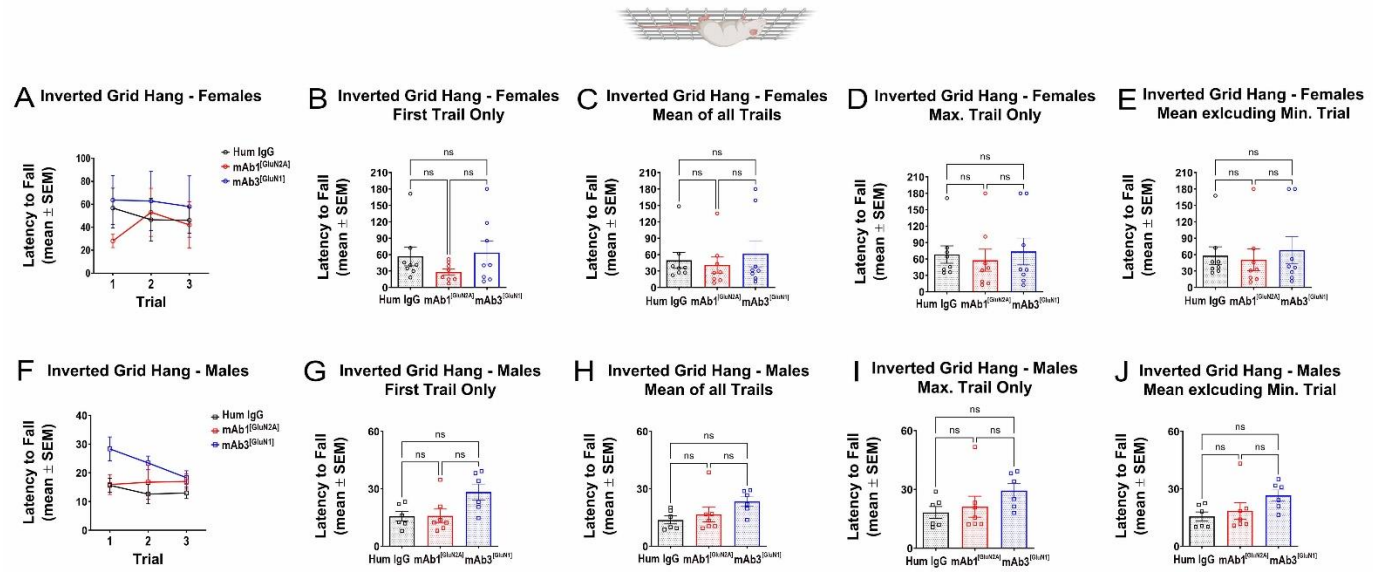

Supplementary Figure 9: No impaired muscle strength and coordination in mAb1[GluN2A] and mAb3[GluN1] treated mice. (A-E) Inverted grid hang of female mice. Human IgG served as controls. (A) No difference of latency to fall in female mice. Human IgG *VS* mAb1[GluN2A]: P = 0.91. Human IgG *VS* mAb3[GluN1]: P = 0.20. (B) No difference of latency to fall (first trail only) in female mice. Human IgG *VS* mAb1[GluN2A]: P = 0.47. Human IgG *VS* mAb3[GluN1]: P > 0.999. (C) No difference of latency to fall (mean of all trails) in female mice. Human IgG *VS* mAb1[GluN2A]: P = 0.97. Human IgG *VS* mAb3[GluN1]: P > 0.999. (D) No difference of latency to fall (max trail only) in female mice. Human IgG *VS* mAb1[GluN2A]: P > 0.999. Human IgG *VS* mAb3[GluN1]: P > 0.999. (E) No difference of latency to fall (mean excluding min trail) in female mice. Human IgG *VS* mAb1[GluN2A]: P > 0.999. Human IgG *VS* mAb3[GluN1]: P > 0.999. (F-J) Inverted grid hang of male mice. (F) significantly increased muscle strength and coordination in mAb3[GluN1] treated male mice across the three trails. Human IgG *VS* mAb1[GluN2A]: P = 0.36. Human IgG *VS* mAb3[GluN1]: P = 0.01. (G) No difference of latency to fall (first trail only) in male mice. Human IgG *VS* mAb1[GluN2A]: P > 0.999. Human IgG *VS* mAb3[GluN1]: P = 0.17. (H) No difference of latency to fall (mean of all trails) in male mice. Human IgG *VS* mAb1[GluN2A]: P > 0.999. Human IgG *VS* mAb3[GluN1]: P = 0.07. (I) No difference of latency to fall (max trail only) in male mice. Human IgG *VS* mAb1[GluN2A]: P > 0.999. Human IgG *VS* mAb3[GluN1]: P = 0.19. (J) No difference of latency to fall (mean excluding min trail) in male mice. Human IgG *VS* mAb1[GluN2A]: P > 0.999. Human IgG *VS* mAb3[GluN1]: P = 0.07.

Supplementary Video 1: Represented balance beam performance of Human IgG treated female in 0.25x speed (trail 4).

Supplementary Video 2: Represented balance beam performance of mAb1$^{[GluN2A]}$ treated female in 0.25x speed (trail 4).

Supplementary Video 3: Represented balance beam performance of mAb3$^{[GluN1]}$ treated female in 0.25x speed (trail 4).

Supplementary Video 4: Represented balance beam performance of Human IgG treated male in 0.25x speed (trail 4).

Supplementary Video 5: Represented balance beam performance of mAb1$^{[GluN2A]}$ treated male in 0.25x speed (trail 4).

Supplementary Video 6: Represented balance beam performance of mAb3$^{[GluN1]}$ treated male in 0.25x speed (trail 4).

Supplementary Video 7: Represented facing up pole performance of Human IgG treated female in 0.5x speed (trail 2).

Supplementary Video 8: Represented facing up pole performance of mAb1$^{[GluN2A]}$ treated female in 0.5x speed (trail 2).

Supplementary Video 9: Represented facing up pole performance of mAb3$^{[GluN1]}$ treated female in 0.5x speed (trail 2).

Supplementary Video 10: Represented facing up pole performance of Human IgG treated male in 0.5x speed (trail 3).

Supplementary Video 11: Represented facing up pole performance of mAb1$^{[GluN2A]}$ treated male in 0.5x speed (trail 3).

Supplementary Video 12: Represented facing up pole performance of mAb3$^{[GluN1]}$ treated male in 0.5x speed (trail 3).

References

1. Dalmau J, Lancaster E, Martinez-Hernandez E, Rosenfeld MR, and Balice-Gordon R. Clinical experience and laboratory investigations in patients with anti-NMDAR encephalitis. *Lancet Neurol.* 2011;10(1):63-74.
2. Dalmau J, Tuzun E, Wu HY, Masjuan J, Rossi JE, Voloschin A, et al. Paraneoplastic anti-N-methyl-D-aspartate receptor encephalitis associated with ovarian teratoma. *Annals of neurology.* 2007;61(1):25-36.
3. Planaguma J, Leypoldt F, Mannara F, Gutierrez-Cuesta J, Martin-Garcia E, Aguilar E, et al. Human N-methyl D-aspartate receptor antibodies alter memory and behaviour in mice. *Brain : a journal of neurology.* 2015;138(Pt 1):94-109.
4. Wurdemann T, Kersten M, Tokay T, Guli X, Kober M, Rohde M, et al. Stereotactic injection of cerebrospinal fluid from anti-NMDA receptor encephalitis into rat dentate gyrus impairs NMDA receptor function. *Brain research.* 2016;1633:10-8.
5. Jones BE, Tovar KR, Goehring A, Jalali-Yazdi F, Okada NJ, Gouaux E, et al. Autoimmune receptor encephalitis in mice induced by active immunization with conformationally stabilized holoreceptors. *Science translational medicine.* 2019;11(500).
6. Hughes EG, Peng X, Gleichman AJ, Lai M, Zhou L, Tsou R, et al. Cellular and synaptic mechanisms of anti-NMDA receptor encephalitis. *The Journal of neuroscience : the official journal of the Society for Neuroscience.* 2010;30(17):5866-75.
7. Ladepeche L, Planaguma J, Thakur S, Suarez I, Hara M, Borbely JS, et al. NMDA Receptor Autoantibodies in Autoimmune Encephalitis Cause a Subunit-Specific Nanoscale Redistribution of NMDA Receptors. *Cell reports.* 2018;23(13):3759-68.
8. Zhou J, Lin Y, Huynh T, Noguchi H, Bush JO, and Pleasure SJ. NMDA receptors control development of somatosensory callosal axonal projections. *Elife.* 2021;10.
9. Varley JA, Webb AJS, Balint B, Fung VSC, Sethi KD, Tijssen MAJ, et al. The Movement disorder associated with NMDAR antibody-encephalitis is complex and characteristic: an expert video-rating study. *Journal of neurology, neurosurgery, and psychiatry.* 2019;90(6):724-6.
10. Bartels F, Krohn S, Nikolaus M, Johannsen J, Wickstrom R, Schimmel M, et al. Clinical and Magnetic Resonance Imaging Outcome Predictors in Pediatric Anti-N-Methyl-D-Aspartate Receptor Encephalitis. *Ann Neurol.* 2020;88(1):148-59.
11. Iwamura Y, Taoka M, and Iriki A. Bilateral activity and callosal connections in the somatosensory cortex. *Neuroscientist.* 2001;7(5):419-29.
12. Paul LK. Developmental malformation of the corpus callosum: a review of typical callosal development and examples of developmental disorders with callosal involvement. *Journal of neurodevelopmental disorders.* 2011;3(1):3-27.
13. Hengst M, Tucke J, Zerres K, Blaum M, and Hausler M. Megalencephaly, mega corpus callosum, and complete lack of motor development: delineation of a rare syndrome. *American journal of medical genetics Part A.* 2010;152A(9):2360-4.
14. Edwards TJ, Sherr EH, Barkovich AJ, and Richards LJ. Clinical, genetic and imaging findings identify new causes for corpus callosum development syndromes. *Brain : a journal of neurology.* 2014;137(Pt 6):1579-613.
15. Semple BD, Blomgren K, Gimlin K, Ferriero DM, and Noble-Haeusslein LJ. Brain development in rodents and humans: Identifying benchmarks of maturation and vulnerability to injury across species. *Progress in neurobiology.* 2013;106-107:1-16.
16. Zhou J, Wen Y, She L, Sui YN, Liu L, Richards LJ, et al. Axon position within the corpus callosum determines contralateral cortical projection. *Proc Natl Acad Sci U S A.* 2013;110(29):E2714-23.

17. Tiller T, Meffre E, Yurasov S, Tsuiji M, Nussenzweig MC, and Wardemann H. Efficient generation of monoclonal antibodies from single human B cells by single cell RT-PCR and expression vector cloning. *J Immunol Methods.* 2008;329(1-2):112-24.
18. Ramberger M, Berretta A, Tan JMM, Sun B, Michael S, Yeo T, et al. Distinctive binding properties of human monoclonal LGI1 autoantibodies determine pathogenic mechanisms. *Brain : a journal of neurology.* 2020.
19. Moscato EH, Peng X, Jain A, Parsons TD, Dalmau J, and Balice-Gordon RJ. Acute mechanisms underlying antibody effects in anti-N-methyl-D-aspartate receptor encephalitis. *Annals of neurology.* 2014;76(1):108-19.
20. Dingledine R, Borges K, Bowie D, and Traynelis SF. The glutamate receptor ion channels. *Pharmacological reviews.* 1999;51(1):7-61.
21. Paoletti P, Bellone C, and Zhou Q. NMDA receptor subunit diversity: impact on receptor properties, synaptic plasticity and disease. *Nature reviews Neuroscience.* 2013;14(6):383-400.
22. Monyer H, Burnashev N, Laurie DJ, Sakmann B, and Seeburg PH. Developmental and regional expression in the rat brain and functional properties of four NMDA receptors. *Neuron.* 1994;12(3):529-40.
23. Sans NA, Montcouquiol ME, and Raymond J. Postnatal developmental changes in AMPA and NMDA receptors in the rat vestibular nuclei. *Brain research Developmental brain research.* 2000;123(1):41-52.
24. Sheng M, Cummings J, Roldan LA, Jan YN, and Jan LY. Changing subunit composition of heteromeric NMDA receptors during development of rat cortex. *Nature.* 1994;368(6467):144-7.
25. Liu XB, Murray KD, and Jones EG. Switching of NMDA receptor 2A and 2B subunits at thalamic and cortical synapses during early postnatal development. *The Journal of neuroscience : the official journal of the Society for Neuroscience.* 2004;24(40):8885-95.
26. Nolt MJ, Lin Y, Hruska M, Murphy J, Sheffler-Colins SI, Kayser MS, et al. EphB controls NMDA receptor function and synaptic targeting in a subunit-specific manner. *J Neurosci.* 2011;31(14):5353-64.
27. Dalva MB, Takasu MA, Lin MZ, Shamah SM, Hu L, Gale NW, et al. EphB receptors interact with NMDA receptors and regulate excitatory synapse formation. *Cell.* 2000;103(6):945-56.
28. Bird AD, and Cuntz H. Dissecting Sholl Analysis into Its Functional Components. *Cell Rep.* 2019;27(10):3081-96 e5.
29. Alcami P, and El Hady A. Axonal Computations. *Front Cell Neurosci.* 2019;13:413.
30. Jirkof P. Burrowing and nest building behavior as indicators of well-being in mice. *J Neurosci Methods.* 2014;234:139-46.
31. Dalmau J. NMDA receptor encephalitis and other antibody-mediated disorders of the synapse: The 2016 Cotzias Lecture. *Neurology.* 2016;87(23):2471-82.
32. Kayser MS, and Dalmau J. Anti-NMDA Receptor Encephalitis in Psychiatry. *Curr Psychiatry Rev.* 2011;7(3):189-93.
33. Heine J, Kopp UA, Klag J, Ploner CJ, Pruss H, and Finke C. Long-Term Cognitive Outcome in Anti-N-Methyl-D-Aspartate Receptor Encephalitis. *Ann Neurol.* 2021;90(6):949-61.
34. Gresa-Arribas N, Titulaer MJ, Torrents A, Aguilar E, McCracken L, Leypoldt F, et al. Antibody titres at diagnosis and during follow-up of anti-NMDA receptor encephalitis: a retrospective study. *Lancet Neurol.* 2014;13(2):167-77.
35. Cai L, Liang Y, Huang H, Zhou X, and Zheng J. Cerebral functional activity and connectivity changes in anti-N-methyl-D-aspartate receptor encephalitis: A resting-state fMRI study. *NeuroImage Clinical.* 2020;25:102189.

36. Peer M, Pruss H, Ben-Dayan I, Paul F, Arzy S, and Finke C. Functional connectivity of large-scale brain networks in patients with anti-NMDA receptor encephalitis: an observational study. *Lancet Psychiatry.* 2017;4(10):768-74.
37. Meixensberger S, Tebartz van Elst L, Schweizer T, Maier SJ, Pruss H, Feige B, et al. Anti-N-Methyl-D-Aspartate-Receptor Encephalitis: A 10-Year Follow-Up. *Frontiers in psychiatry.* 2020;11:245.
38. Castillo-Gomez E, Oliveira B, Tapken D, Bertrand S, Klein-Schmidt C, Pan H, et al. All naturally occurring autoantibodies against the NMDA receptor subunit NR1 have pathogenic potential irrespective of epitope and immunoglobulin class. *Mol Psychiatry.* 2017;22(12):1776-84.
39. Wollmuth LP, Chan K, and Groc L. The diverse and complex modes of action of anti-NMDA receptor autoantibodies. *Neuropharmacology.* 2021;194:108624.
40. Diamond B. Antibodies and the Brain: Lessons from Lupus. *J Immunol.* 2010;185(5):2637-40.
41. Kreye J, Wenke NK, Chayka M, Leubner J, Murugan R, Maier N, et al. Human cerebrospinal fluid monoclonal N-methyl-D-aspartate receptor autoantibodies are sufficient for encephalitis pathogenesis. *Brain.* 2016;139(Pt 10):2641-52.
42. Husebye ES, Sthoeger ZM, Dayan M, Zinger H, Elbirt D, Levite M, et al. Autoantibodies to a NR2A peptide of the glutamate/NMDA receptor in sera of patients with systemic lupus erythematosus. *Ann Rheum Dis.* 2005;64(8):1210-3.
43. Yang Y, Yuan C, Shen SQ, Wang XE, Mei QH, Jiang WQ, et al. Autoantibodies to NR2A Peptide of the Glutamate/NMDA Receptor in Patients with Seizure Disorders in Neuropsychiatric Systemic Lupus Erythematosus. *Mediators Inflamm.* 2017;2017:5047898.
44. Yoshio T, Onda K, Nara H, and Minota S. Association of IgG anti-NR2 glutamate receptor antibodies in cerebrospinal fluid with neuropsychiatric systemic lupus erythematosus. *Arthritis Rheum.* 2006;54(2):675-8.
45. Harrison MJ, Ravdin LD, and Lockshin MD. Relationship between serum NR2a antibodies and cognitive dysfunction in systemic lupus erythematosus. *Arthritis Rheum.* 2006;54(8):2515-22.
46. Iwamura Y. Bilateral receptive field neurons and callosal connections in the somatosensory cortex. *Philos Trans R Soc Lond B Biol Sci.* 2000;355(1394):267-73.
47. Endres D, Rauer S, Kern W, Venhoff N, Maier SJ, Runge K, et al. Psychiatric Presentation of Anti-NMDA Receptor Encephalitis. *Front Neurol.* 2019;10:1086.
48. Chung WS, and Barres BA. The role of glial cells in synapse elimination. *Curr Opin Neurobiol.* 2012;22(3):438-45.
49. Rigby MJ, Gomez TM, and Puglielli L. Glial Cell-Axonal Growth Cone Interactions in Neurodevelopment and Regeneration. *Front Neurosci.* 2020;14:203.
50. Chowen JA, and Garcia-Segura LM. Role of glial cells in the generation of sex differences in neurodegenerative diseases and brain aging. *Mech Ageing Dev.* 2021;196:111473.
51. Eggers EL, Michel BA, Wu H, Wang S-z, Bevan CJ, Abounasr A, et al. Clonal relationships of CSF B cells in treatment-naive multiple sclerosis patients. *JCI Insight.* 2017;2(22).
52. Picelli S, Faridani OR, Björklund ÅK, Winberg G, Sagasser S, and Sandberg R. Full-length RNA-seq from single cells using Smart-seq2. *Nature Protocols.* 2014;9:171.
53. Tiller T, Meffre E, Yurasov S, Tsuiji M, Nussenzweig MC, and Wardemann H. Efficient generation of monoclonal antibodies from single human B cells by single cell RT-PCR and expression vector cloning. *Journal of immunological methods.* 2008;329(1-2):112-24.
54. Vogt D, Wu PR, Sorrells SF, Arnold C, Alvarez-Buylla A, and Rubenstein JL. Viral-mediated Labeling and Transplantation of Medial Ganglionic Eminence (MGE) Cells for In Vivo Studies. *Journal of visualized experiments : JoVE.* 2015(98).